Sensitizing triple negative breast cancer to approved therapies: Design, synthesis and biological activity of MNK inhibitors

Elisabeth Bou Petit

ANNEX

ANNEX 2

X-ray crystallographic data

Compound 64{1,4,3}

A single monocrystal was obtained from a solution of 5 mg of the crystalline compound **64**{*1*,*4*,*3*} in 3 mL of methanol introduced in a tube closed in a flask containing an antisolvent (water). After two weeks, methanol was partially evaporated and a monoclinic yellow prism-like specimen of **64**{*1*,*4*,*3*} was obtained. Such monocrystal was sent to C. Puigjaner of the Unitat de Difracció de RX. Centres Científics i Tecnològics de la Universitat de Barcelona (CCiTUB). Universitat de Barcelona for the corresponding X-ray crystallographic analysis.

Crystal Structure Report

A yellow prism-like specimen of $C_{19}H_{18}N_4O_2$, approximate dimensions 0.126 mm x 0.135 mm x 0.195 mm, was used for the X-ray crystallographic analysis. The X-ray intensity data were measured on a D8 Venture system equipped with a multilayer monochromator and a Mo microfocus (λ = 0.71073 Å).

The frames were integrated with the Bruker SAINT software package using a narrow-frame algorithm. The integration of the data using a monoclinic unit cell yielded a total of 10497 reflections to a maximum θ angle of 23.32° (0.90 Å resolution), of which 2574 were independent (average redundancy 4.078, completeness = 99.2%, R_{int} = 4.36%, R_{sig} = 3.65%) and 2038 (79.18%) were greater than $2\sigma(F^2)$. The final cell constants of a = 9.1249(8) Å, b = 12.6511(12) Å, c = 16.0895(16) Å, β = 105.091(3)°, volume = 1793.3(3) $Å^3$, are based upon the refinement of the XYZ-centroids of reflections above 20 σ(I). Data were corrected for absorption effects using the multi-scan method (SADABS). The calculated minimum and maximum transmission coefficients (based on crystal size) are 0.6710 and 0.7449.
The structure was solved and refined using the Bruker SHELXTL Software Package, using the space group P 1 21/n 1, with Z = 4 for the formula unit, $C_{19}H_{18}N_4O_2$. The final anisotropic full-matrix least-squares refinement on F^2 with 227 variables converged at R1 = 5.17%, for the observed data and wR2 = 15.96% for all data. The goodness-of-fit was 1.100. The largest peak in the final difference electron density synthesis was 0.430 $e^-/Å^3$ and the largest hole was -0.288 $e^-/Å^3$ with an RMS deviation of 0.075 $e^-/Å^3$. On the basis of the final model, the calculated density was 1.238 g/cm^3 and F(000), 704 e^-.

Atomic coordinates (x 10^4) and equivalent isotropic displacement parameters ($Å^2$x 10^3) for mo_023UB60_0m. U(eq) is defined as one third of the trace of the orthogonalized U^{ij} tensor.

	x	y	z	U(eq)
O(1)	6924(2)	323(2)	7212(1)	40(1)
O(2)	3766(2)	5632(2)	6717(1)	34(1)
N(1)	1671(2)	4739(2)	6033(2)	26(1)
N(2)	-622(2)	3800(2)	5418(1)	27(1)
N(3)	-1206(3)	2866(2)	5672(2)	29(1)
N(4)	-629(3)	1567(2)	6780(2)	44(1)
C(1)	7668(3)	-317(2)	7927(2)	42(1)
C(2)	5855(3)	1036(2)	7328(2)	30(1)
C(3)	5531(3)	1239(2)	8110(2)	30(1)
C(4)	4376(3)	1945(2)	8132(2)	28(1)
C(5)	3533(3)	2453(2)	7404(2)	26(1)
C(6)	3911(3)	2257(2)	6630(2)	32(1)
C(7)	5068(3)	1562(2)	6596(2)	34(1)
C(8)	2265(3)	3201(2)	7458(2)	26(1)
C(9)	2797(3)	4361(2)	7561(2)	27(1)
C(10)	2813(3)	4947(2)	6739(2)	27(1)
C(11)	654(3)	3924(2)	6035(2)	24(1)
C(12)	911(3)	3163(2)	6685(2)	25(1)
C(13)	-309(3)	2479(2)	6421(2)	28(1)
C(14)	-2593(4)	2447(3)	5163(2)	37(1)
C(15)	-3834(4)	3079(3)	4912(2)	58(1)
C(16)	-5197(5)	2652(5)	4409(3)	94(2)
C(17)	-5264(7)	1618(6)	4190(3)	103(2)
C(18)	-4018(7)	974(4)	4433(3)	86(2)
C(19)	-2662(5)	1384(3)	4916(2)	55(1)

Bond lengths [Å] and angles [°] for mo_023UB60_0m. Symmetry transformations used to generate equivalent atoms:

O(1)-C(2)	1.377(3)	C(2)-C(7)	1.381(4)	C(9)-H(9A)	0.99
O(1)-C(1)	1.426(4)	C(2)-C(3)	1.389(4)	C(9)-H(9B)	0.99
O(2)-C(10)	1.235(3)	C(3)-C(4)	1.390(4)	C(11)-C(12)	1.396(4)
N(1)-C(10)	1.353(4)	C(3)-H(3)	0.95	C(12)-C(13)	1.386(4)
N(1)-C(11)	1.388(3)	C(4)-C(5)	1.382(4)	C(14)-C(15)	1.358(5)
N(1)-H(1N)	0.88	C(4)-H(4)	0.95	C(14)-C(19)	1.399(5)
N(2)-C(11)	1.328(3)	C(5)-C(6)	1.397(4)	C(15)-C(16)	1.404(5)
N(2)-N(3)	1.401(3)	C(5)-C(8)	1.515(4)	C(15)-H(15)	0.95
N(3)-C(13)	1.361(4)	C(6)-C(7)	1.386(4)	C(16)-C(17)	1.352(8)
N(3)-C(14)	1.419(4)	C(6)-H(6)	0.95	C(16)-H(16)	0.95
N(4)-C(13)	1.355(4)	C(7)-H(7)	0.95	C(17)-C(18)	1.370(8)
N(4)-H(4NA)	0.88	C(8)-C(12)	1.508(4)	C(17)-H(17)	0.95
N(4)-H(4NB)	0.88	C(8)-C(9)	1.541(4)	C(18)-C(19)	1.380(6)
C(1)-H(1A)	0.98	C(8)-H(8)	1	C(18)-H(18)	0.95
C(1)-H(1B)	0.98	C(9)-C(10)	1.520(4)	C(19)-H(19)	0.95
C(1)-H(1C)	0.98				

C(2)-O(1)-C(1)	117.8(2)	C(4)-C(5)-C(6)	117.5(3)	N(1)-C(11)-C(12)	122.2(2)
C(10)-N(1)-C(11)	120.8(2)	C(4)-C(5)-C(8)	120.4(3)	C(13)-C(12)-C(11)	103.7(2)
C(10)-N(1)-H(1N)	119.6	C(6)-C(5)-C(8)	122.1(2)	C(13)-C(12)-C(8)	133.8(2)
C(11)-N(1)-H(1N)	119.6	C(7)-C(6)-C(5)	121.0(3)	C(11)-C(12)-C(8)	122.5(2)
C(11)-N(2)-N(3)	102.0(2)	C(7)-C(6)-H(6)	119.5	N(4)-C(13)-N(3)	122.5(3)
C(13)-N(3)-N(2)	112.0(2)	C(5)-C(6)-H(6)	119.5	N(4)-C(13)-C(12)	130.2(3)
C(13)-N(3)-C(14)	128.2(2)	C(2)-C(7)-C(6)	120.3(3)	N(3)-C(13)-C(12)	107.3(2)
N(2)-N(3)-C(14)	119.8(2)	C(2)-C(7)-H(7)	119.9	C(15)-C(14)-C(19)	120.6(3)
C(13)-N(4)-H(4NA)	120	C(6)-C(7)-H(7)	119.9	C(15)-C(14)-N(3)	120.1(3)
C(13)-N(4)-H(4NB)	120	C(12)-C(8)-C(5)	114.0(2)	C(19)-C(14)-N(3)	119.3(3)
H(4NA)-N(4)-H(4NB)	120	C(12)-C(8)-C(9)	106.7(2)	C(14)-C(15)-C(16)	119.3(4)
O(1)-C(1)-H(1A)	109.5	C(5)-C(8)-C(9)	112.2(2)	C(14)-C(15)-H(15)	120.3
O(1)-C(1)-H(1B)	109.5	C(12)-C(8)-H(8)	107.9	C(16)-C(15)-H(15)	120.3
H(1A)-C(1)-H(1B)	109.5	C(5)-C(8)-H(8)	107.9	C(17)-C(16)-C(15)	119.7(5)
O(1)-C(1)-H(1C)	109.5	C(9)-C(8)-H(8)	107.9	C(17)-C(16)-H(16)	120.2
H(1A)-C(1)-H(1C)	109.5	C(10)-C(9)-C(8)	116.4(2)	C(15)-C(16)-H(16)	120.2
H(1B)-C(1)-H(1C)	109.5	C(10)-C(9)-H(9A)	108.2	C(16)-C(17)-C(18)	121.5(4)
O(1)-C(2)-C(7)	115.4(3)	C(8)-C(9)-H(9A)	108.2	C(16)-C(17)-H(17)	119.2
O(1)-C(2)-C(3)	124.7(3)	C(10)-C(9)-H(9B)	108.2	C(18)-C(17)-H(17)	119.2
C(7)-C(2)-C(3)	119.8(3)	C(8)-C(9)-H(9B)	108.2	C(17)-C(18)-C(19)	119.6(5)
C(2)-C(3)-C(4)	119.0(3)	H(9A)-C(9)-H(9B)	107.3	C(17)-C(18)-H(18)	120.2
C(2)-C(3)-H(3)	120.5	O(2)-C(10)-N(1)	120.4(3)	C(19)-C(18)-H(18)	120.2
C(4)-C(3)-H(3)	120.5	O(2)-C(10)-C(9)	122.3(2)	C(18)-C(19)-C(14)	119.2(5)
C(5)-C(4)-C(3)	122.3(3)	N(1)-C(10)-C(9)	117.2(2)	C(18)-C(19)-H(19)	120.4
C(5)-C(4)-H(4)	118.8	N(2)-C(11)-N(1)	122.8(2)	C(14)-C(19)-H(19)	120.4
C(3)-C(4)-H(4)	118.8	N(2)-C(11)-C(12)	115.0(2)		

Anisotropic displacement parameters ($Å^2 x\ 10^3$) for mo_023UB60_0m. The anisotropic displacement factor exponent takes the form: $-2\pi^2[\ h^2\ a^{*2}U^{11} + ...\ + 2\ h\ k\ a^*\ b^*\ U^{12}\ ]$

	U^{11}	U^{22}	U^{33}	U^{23}	U^{13}	U^{12}
O(1)	34(1)	34(1)	59(2)	9(1)	24(1)	5(1)
O(2)	31(1)	32(1)	36(1)	1(1)	5(1)	-9(1)
N(1)	27(1)	25(1)	24(1)	5(1)	3(1)	-7(1)
N(2)	27(1)	26(1)	26(1)	7(1)	4(1)	-8(1)
N(3)	27(1)	28(1)	30(1)	6(1)	5(1)	-10(1)
N(4)	36(2)	38(2)	51(2)	21(1)	-1(1)	-14(1)
C(1)	31(2)	37(2)	59(2)	6(2)	11(2)	6(1)
C(2)	23(2)	27(2)	43(2)	3(1)	12(1)	-4(1)
C(3)	25(2)	29(2)	33(2)	7(1)	1(1)	-3(1)
C(4)	26(2)	31(2)	27(2)	2(1)	6(1)	-2(1)
C(5)	23(2)	27(2)	28(2)	3(1)	5(1)	-6(1)
C(6)	35(2)	34(2)	28(2)	8(1)	10(1)	-1(1)
C(7)	35(2)	37(2)	36(2)	3(1)	18(2)	0(1)
C(8)	26(2)	30(2)	22(2)	4(1)	6(1)	0(1)
C(9)	26(2)	30(2)	22(2)	-1(1)	3(1)	1(1)
C(10)	25(2)	26(2)	31(2)	-3(1)	8(1)	-1(1)
C(11)	22(2)	24(1)	25(2)	4(1)	4(1)	-2(1)
C(12)	23(1)	24(1)	28(2)	4(1)	6(1)	0(1)
C(13)	26(2)	27(2)	28(2)	10(1)	5(1)	0(1)
C(14)	39(2)	50(2)	20(2)	7(1)	2(1)	-24(2)
C(15)	37(2)	71(3)	54(2)	39(2)	-10(2)	-24(2)
C(16)	52(3)	132(5)	75(3)	75(3)	-25(2)	-48(3)
C(17)	100(4)	159(6)	31(2)	37(3)	-19(3)	-98(4)
C(18)	127(4)	103(4)	31(2)	-21(2)	29(3)	-90(4)
C(19)	80(3)	59(2)	35(2)	-12(2)	30(2)	-40(2)

Hydrogen coordinates (x 10^4) and isotropic displacement parameters ($Å^2$x 10^3)
for mo_023UB60_0m.

	x	y	z	U(eq)
H(1N)	1573	5125	5566	31
H(4NA)	-1443	1201	6527	66
H(4NB)	-23	1340	7266	66
H(1A)	8288	133	8380	63
H(1B)	8320	-833	7743	63
H(1C)	6907	-688	8149	63
H(3)	6090	900	8621	36
H(4)	4157	2084	8668	34
H(6)	3366	2605	6120	39
H(7)	5321	1448	6066	41
H(8)	1914	3004	7976	31
H(9A)	2130	4753	7851	32
H(9B)	3836	4379	7949	32
H(15)	-3779	3802	5077	70
H(16)	-6068	3088	4222	113
H(17)	-6197	1331	3861	124
H(18)	-4087	251	4269	103
H(19)	-1785	950	5079	66

Torsion angles [°] for mo_023UB60_0m.

C(11)-N(2)-N(3)-C(13)	1.3(3)	N(2)-C(11)-C(12)-C(13)	2.4(3)
C(11)-N(2)-N(3)-C(14)	-179.4(3)	N(1)-C(11)-C(12)-C(13)	-176.9(2)
C(1)-O(1)-C(2)-C(7)	-174.1(2)	N(2)-C(11)-C(12)-C(8)	-177.3(2)
C(1)-O(1)-C(2)-C(3)	5.4(4)	N(1)-C(11)-C(12)-C(8)	3.4(4)
O(1)-C(2)-C(3)-C(4)	-177.2(2)	C(5)-C(8)-C(12)-C(13)	79.1(4)
C(7)-C(2)-C(3)-C(4)	2.2(4)	C(9)-C(8)-C(12)-C(13)	-156.5(3)
C(2)-C(3)-C(4)-C(5)	0.2(4)	C(5)-C(8)-C(12)-C(11)	-101.3(3)
C(3)-C(4)-C(5)-C(6)	-1.9(4)	C(9)-C(8)-C(12)-C(11)	23.1(3)
C(3)-C(4)-C(5)-C(8)	178.8(2)	N(2)-N(3)-C(13)-N(4)	-178.3(3)
C(4)-C(5)-C(6)-C(7)	1.3(4)	C(14)-N(3)-C(13)-N(4)	2.5(5)
C(8)-C(5)-C(6)-C(7)	-179.5(3)	N(2)-N(3)-C(13)-C(12)	0.1(3)
O(1)-C(2)-C(7)-C(6)	176.6(2)	C(14)-N(3)-C(13)-C(12)	-179.2(3)
C(3)-C(2)-C(7)-C(6)	-2.9(4)	C(11)-C(12)-C(13)-N(4)	176.9(3)
C(5)-C(6)-C(7)-C(2)	1.1(4)	C(8)-C(12)-C(13)-N(4)	-3.5(5)
C(4)-C(5)-C(8)-C(12)	-143.6(3)	C(11)-C(12)-C(13)-N(3)	-1.4(3)
C(6)-C(5)-C(8)-C(12)	37.2(4)	C(8)-C(12)-C(13)-N(3)	178.3(3)
C(4)-C(5)-C(8)-C(9)	95.0(3)	C(13)-N(3)-C(14)-C(15)	128.9(3)
C(6)-C(5)-C(8)-C(9)	-84.2(3)	N(2)-N(3)-C(14)-C(15)	-50.3(4)
C(12)-C(8)-C(9)-C(10)	-42.0(3)	C(13)-N(3)-C(14)-C(19)	-51.7(4)
C(5)-C(8)-C(9)-C(10)	83.5(3)	N(2)-N(3)-C(14)-C(19)	129.1(3)
C(11)-N(1)-C(10)-O(2)	175.8(2)	C(19)-C(14)-C(15)-C(16)	0.6(5)
C(11)-N(1)-C(10)-C(9)	-8.4(4)	N(3)-C(14)-C(15)-C(16)	180.0(3)
C(8)-C(9)-C(10)-O(2)	-146.6(3)	C(14)-C(15)-C(16)-C(17)	1.0(6)
C(8)-C(9)-C(10)-N(1)	37.7(3)	C(15)-C(16)-C(17)-C(18)	-1.5(7)
N(3)-N(2)-C(11)-N(1)	177.0(2)	C(16)-C(17)-C(18)-C(19)	0.4(7)
N(3)-N(2)-C(11)-C(12)	-2.3(3)	C(17)-C(18)-C(19)-C(14)	1.1(5)
C(10)-N(1)-C(11)-N(2)	168.4(2)	C(15)-C(14)-C(19)-C(18)	-1.7(5)
C(10)-N(1)-C(11)-C(12)	-12.4(4)	N(3)-C(14)-C(19)-C(18)	179.0(3)

Symmetry transformations used to generate equivalent atoms:

Compound **84{*3,1,3*}**

A single monocrystal was obtained from a solution of 2 mg of the crystalline compound **84**{*3*,*1*,*3*} in 1 mL of methanol introduced in a tube closed in a flask containing an antisolvent (water). After two weeks, methanol was partially evaporated and a monoclinic orange prism-like specimen of **84**{*3*,*1*,*3*} was obtained. Such monocrystal was submitted to Dr. Cristina Puigjaner of the Unitat de Difracció de RX. Centres Científics i Tecnològics de la Universitat de Barcelona (CCiTUB). Universitat de Barcelona. for the corresponding X-ray crystallographic analysis.

Crystal Structure Report

A orange prism-like specimen of $C_{18}H_{14}N_4O$, approximate dimensions 0.066 mm x 0.130 mm x 0.292 mm, was used for the X-ray crystallographic analysis. The X-ray intensity data were measured on a D8 Venture system equipped with a multilayer monochromator and a Mo microfocus (λ = 0.71073 Å).

The frames were integrated with the Bruker SAINT software package using a narrow-frame algorithm. The integration of the data using a monoclinic unit cell yielded a total of 24789 reflections to a maximum θ angle of 27.61° (0.77 Å resolution), of which 3348 were independent (average redundancy 7.404, completeness = 99.1%, R_{int} = 4.76%, R_{sig} = 2.60%) and 2631 (78.58%) were greater than $2\sigma(F^2)$. The final cell constants of a = 27.7141(13) Å, b = 6.4562(3) Å, c = 20.6251(10) Å, β = 128.1800(10)°, volume = 2900.9(2) $Å^3$, are based upon the refinement of the XYZ-centroids of reflections above 20 σ(I). Data were corrected for absorption effects using the multi-scan method (SADABS). The calculated minimum and maximum transmission coefficients (based on crystal size) are 0.6825 and 0.7456.

The structure was solved and refined using the Bruker SHELXTL Software Package, using the space group C 1 2/c 1, with Z = 8 for the formula unit, $C_{18}H_{14}N_4O$. The final anisotropic full-matrix least-squares refinement on F^2 with 216 variables converged at R1 = 4.91%, for the observed data and wR2 = 14.76% for all data. The goodness-of-fit was 1.063. The largest peak in the final difference electron density synthesis was 0.404 $e^-/Å^3$ and the largest hole was -0.270 $e^-/Å^3$ with an RMS deviation of 0.055 $e^-/Å^3$. On the basis of the final model, the calculated density was 1.384 g/cm^3 and F(000), 1264 e^-.

Atomic coordinates (x 10^4) and equivalent isotropic displacement parameters ($Å^2$x 10^3) for mo_023WB46_0m_a. U(eq) is defined as one third of the trace of the orthogonalized U^{ij} tensor.

	x	y	z	U(eq)
O(1)	2935(1)	8892(2)	5851(1)	33(1)
N(1)	3278(1)	7044(2)	5280(1)	25(1)
N(2)	3731(1)	5226(2)	4732(1)	22(1)
N(3)	4254(1)	5497(2)	4779(1)	23(1)
N(4)	5079(1)	7858(2)	5439(1)	29(1)
C(1)	4231(1)	13272(3)	6897(1)	35(1)
C(2)	4335(1)	14701(3)	7481(1)	46(1)
C(3)	4232(1)	14154(4)	8032(1)	47(1)
C(4)	4020(1)	12202(4)	8010(1)	42(1)
C(5)	3909(1)	10769(3)	7430(1)	34(1)
C(6)	4018(1)	11292(3)	6871(1)	28(1)
C(7)	3926(1)	9752(3)	6270(1)	25(1)
C(8)	4337(1)	9490(3)	6114(1)	24(1)
C(9)	4230(1)	7949(2)	5552(1)	21(1)
C(10)	3713(1)	6710(2)	5179(1)	21(1)
C(11)	3357(1)	8563(3)	5809(1)	26(1)
C(12)	4544(1)	7127(2)	5262(1)	21(1)
C(13)	3331(1)	3532(2)	4277(1)	22(1)
C(14)	2986(1)	2663(3)	4486(1)	27(1)
C(15)	2592(1)	1031(3)	4026(1)	31(1)
C(16)	2558(1)	211(3)	3379(1)	33(1)
C(17)	2918(1)	1050(3)	3187(1)	34(1)
C(18)	3300(1)	2720(3)	3626(1)	28(1)

Bond lengths [Å] and angles [°] for mo_023WB46_0m_a.

O(1)-C(11)	1.243(2)	C(2)-C(3)	1.379(3)	C(9)-C(10)	1.386(2)
N(1)-C(10)	1.361(2)	C(2)-H(2)	0.95	C(9)-C(12)	1.427(2)
N(1)-C(11)	1.380(2)	C(3)-C(4)	1.380(3)	C(13)-C(14)	1.390(2)
N(1)-H(1N)	0.88	C(3)-H(3)	0.95	C(13)-C(18)	1.394(2)
N(2)-C(10)	1.352(2)	C(4)-C(5)	1.388(3)	C(14)-C(15)	1.386(2)
N(2)-N(3)	1.4013(18)	C(4)-H(4)	0.95	C(14)-H(14)	0.95
N(2)-C(13)	1.421(2)	C(5)-C(6)	1.404(3)	C(15)-C(16)	1.384(3)
N(3)-C(12)	1.325(2)	C(5)-H(5)	0.95	C(15)-H(15)	0.95
N(4)-C(12)	1.375(2)	C(6)-C(7)	1.483(2)	C(16)-C(17)	1.389(3)
N(4)-H(4NA)	0.90(2)	C(7)-C(8)	1.370(2)	C(16)-H(16)	0.95
N(4)-H(4NB)	0.91(3)	C(7)-C(11)	1.459(2)	C(17)-C(18)	1.385(2)
C(1)-C(6)	1.394(3)	C(8)-C(9)	1.414(2)	C(17)-H(17)	0.95
C(1)-C(2)	1.397(3)	C(8)-H(8)	0.95	C(18)-H(18)	0.95
C(1)-H(1)	0.95				

C(10)-N(1)-C(11)	120.77(13)	C(4)-C(5)-C(6)	120.2(2)	N(3)-C(12)-N(4)	121.62(14)
C(10)-N(1)-H(1N)	119.6	C(4)-C(5)-H(5)	119.9	N(3)-C(12)-C(9)	111.61(14)
C(11)-N(1)-H(1N)	119.6	C(6)-C(5)-H(5)	119.9	N(4)-C(12)-C(9)	126.77(15)
C(10)-N(2)-N(3)	109.69(12)	C(1)-C(6)-C(5)	119.24(17)	C(14)-C(13)-C(18)	120.23(15)
C(10)-N(2)-C(13)	130.78(13)	C(1)-C(6)-C(7)	119.90(17)	C(14)-C(13)-N(2)	120.77(14)
N(3)-N(2)-C(13)	119.51(12)	C(5)-C(6)-C(7)	120.85(17)	C(18)-C(13)-N(2)	118.99(15)
C(12)-N(3)-N(2)	105.69(12)	C(8)-C(7)-C(11)	120.20(15)	C(15)-C(14)-C(13)	119.69(15)
C(12)-N(4)-H(4NA)	116.2(14)	C(8)-C(7)-C(6)	122.59(15)	C(15)-C(14)-H(14)	120.2
C(12)-N(4)-H(4NB)	121.1(19)	C(11)-C(7)-C(6)	117.14(14)	C(13)-C(14)-H(14)	120.2
H(4NA)-N(4)-H(4NB)	122(2)	C(7)-C(8)-C(9)	119.72(15)	C(16)-C(15)-C(14)	120.49(16)
C(6)-C(1)-C(2)	119.8(2)	C(7)-C(8)-H(8)	120.1	C(16)-C(15)-H(15)	119.8
C(6)-C(1)-H(1)	120.1	C(9)-C(8)-H(8)	120.1	C(14)-C(15)-H(15)	119.8
C(2)-C(1)-H(1)	120.1	C(10)-C(9)-C(8)	118.81(14)	C(15)-C(16)-C(17)	119.49(16)
C(3)-C(2)-C(1)	120.1(2)	C(10)-C(9)-C(12)	103.91(14)	C(15)-C(16)-H(16)	120.3
C(3)-C(2)-H(2)	119.9	C(8)-C(9)-C(12)	137.13(15)	C(17)-C(16)-H(16)	120.3
C(1)-C(2)-H(2)	119.9	N(2)-C(10)-N(1)	128.78(14)	C(18)-C(17)-C(16)	120.75(17)
C(2)-C(3)-C(4)	120.62(18)	N(2)-C(10)-C(9)	109.05(14)	C(18)-C(17)-H(17)	119.6
C(2)-C(3)-H(3)	119.7	N(1)-C(10)-C(9)	122.17(14)	C(16)-C(17)-H(17)	119.6
C(4)-C(3)-H(3)	119.7	O(1)-C(11)-N(1)	118.75(15)	C(17)-C(18)-C(13)	119.30(16)
C(3)-C(4)-C(5)	119.9(2)	O(1)-C(11)-C(7)	123.35(15)	C(17)-C(18)-H(18)	120.4
C(3)-C(4)-H(4)	120	N(1)-C(11)-C(7)	117.86(14)	C(13)-C(18)-H(18)	120.4
C(5)-C(4)-H(4)	120				

Symmetry transformations used to generate equivalent atoms:

Anisotropic displacement parameters ($Å^2 x\ 10^3$) for mo_023WB46_0m_a. The anisotropic displacement factor exponent takes the form: $-2\pi^2[\ h^2\ a^{*2}U^{11} + ...\ + 2\ h\ k\ a^*\ b^*\ U^{12}\ ]$

	U^{11}	U^{22}	U^{33}	U^{23}	U^{13}	U^{12}
O(1)	22(1)	46(1)	38(1)	-20(1)	22(1)	-9(1)
N(1)	17(1)	32(1)	29(1)	-12(1)	16(1)	-7(1)
N(2)	18(1)	26(1)	27(1)	-5(1)	17(1)	-2(1)
N(3)	19(1)	26(1)	29(1)	-2(1)	18(1)	-1(1)
N(4)	24(1)	28(1)	46(1)	-7(1)	27(1)	-4(1)
C(1)	23(1)	37(1)	39(1)	-12(1)	17(1)	-3(1)
C(2)	29(1)	41(1)	59(1)	-24(1)	23(1)	-7(1)
C(3)	26(1)	59(1)	47(1)	-31(1)	18(1)	-2(1)
C(4)	26(1)	64(1)	30(1)	-15(1)	15(1)	4(1)
C(5)	25(1)	44(1)	30(1)	-9(1)	16(1)	-1(1)
C(6)	15(1)	35(1)	28(1)	-13(1)	10(1)	-2(1)
C(7)	18(1)	28(1)	25(1)	-7(1)	12(1)	-2(1)
C(8)	15(1)	28(1)	26(1)	-5(1)	11(1)	-2(1)
C(9)	16(1)	25(1)	25(1)	-2(1)	14(1)	-1(1)
C(10)	18(1)	25(1)	23(1)	-4(1)	14(1)	-1(1)
C(11)	20(1)	33(1)	28(1)	-9(1)	16(1)	-4(1)
C(12)	19(1)	22(1)	24(1)	1(1)	14(1)	2(1)
C(13)	18(1)	24(1)	23(1)	-3(1)	12(1)	-1(1)
C(14)	28(1)	30(1)	29(1)	-6(1)	21(1)	-4(1)
C(15)	31(1)	30(1)	38(1)	-4(1)	25(1)	-6(1)
C(16)	32(1)	31(1)	34(1)	-10(1)	20(1)	-10(1)
C(17)	35(1)	40(1)	31(1)	-12(1)	22(1)	-7(1)
C(18)	28(1)	35(1)	29(1)	-5(1)	22(1)	-4(1)

Hydrogen coordinates (x 10^4) and isotropic displacement parameters ($Å^2$x 10^3)
for mo_023WB46_0m_a.

	x	y	z	U(eq)
H(1N)	2943	6283	5005	30
H(4NA)	5254(10)	7050(40)	5282(13)	36(6)
H(4NB)	5215(14)	9170(50)	5636(18)	69(8)
H(1)	4304	13648	6520	42
H(2)	4478	16053	7498	55
H(3)	4307	15131	8429	56
H(4)	3950	11839	8392	50
H(5)	3758	9431	7412	41
H(8)	4692	10341	6384	28
H(14)	3019	3185	4943	32
H(15)	2344	471	4155	37
H(16)	2291	-917	3068	40
H(17)	2902	471	2751	41
H(18)	3538	3306	3484	34

Experimental determination of the energetic barriers by **DSC**

Activation energy determination from DSC curves

Step 1

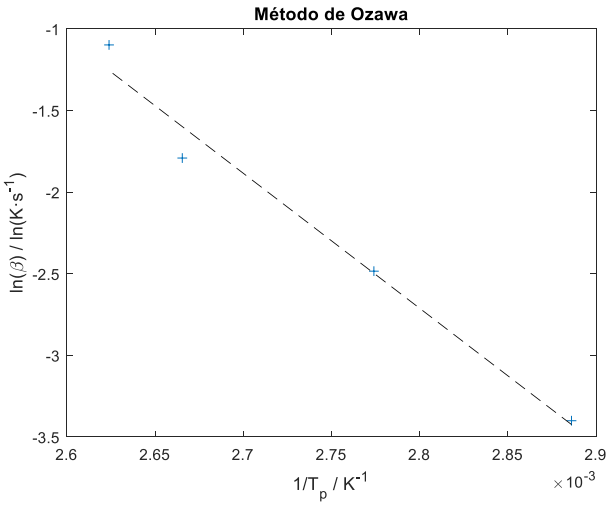

E_a=15.643 ± 1.64 kcal·mol^{-1}

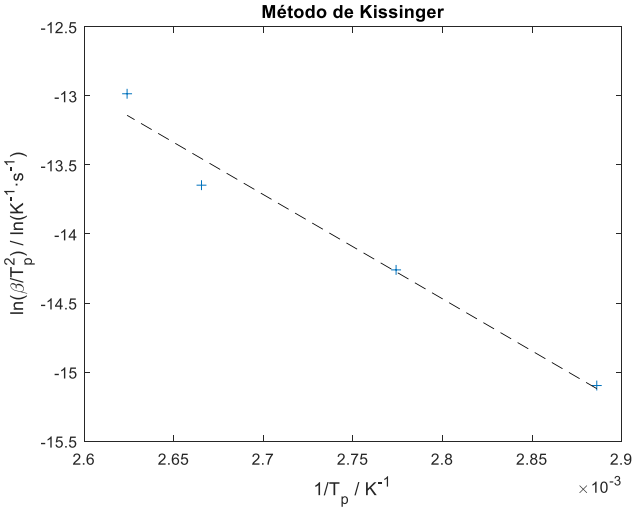

E_a=14.269 ± 1.63 kcal·mol^{-1}

Figure 9.1. Results from the application of different kinetic methods for step 1

Step 2

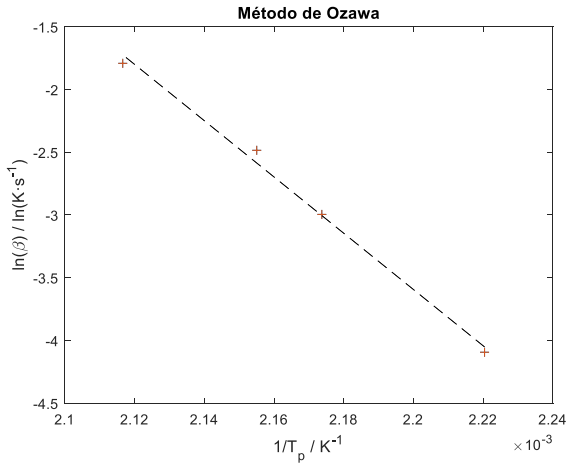

E_a=42.395 ± 2.3 kcal·mol^{-1}

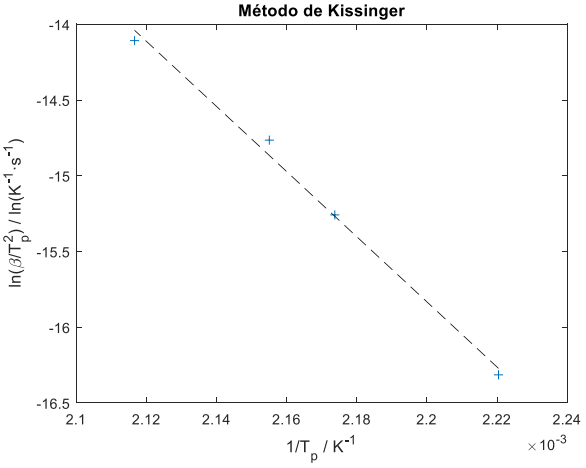

E_a=42.766 ± 2.4 kcal·mol^{-1}

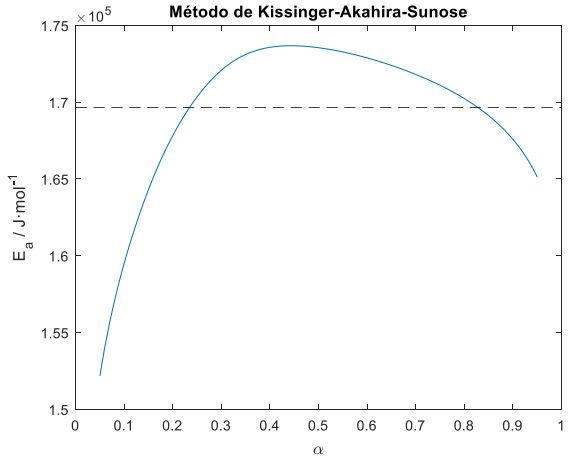

E_a=40.587 ± 0.23 kcal·mol^{-1}

Figure 9.2. Results from the application of different kinetic methods for step 2

Spectroscopy of compound 82{*2,1,3*}

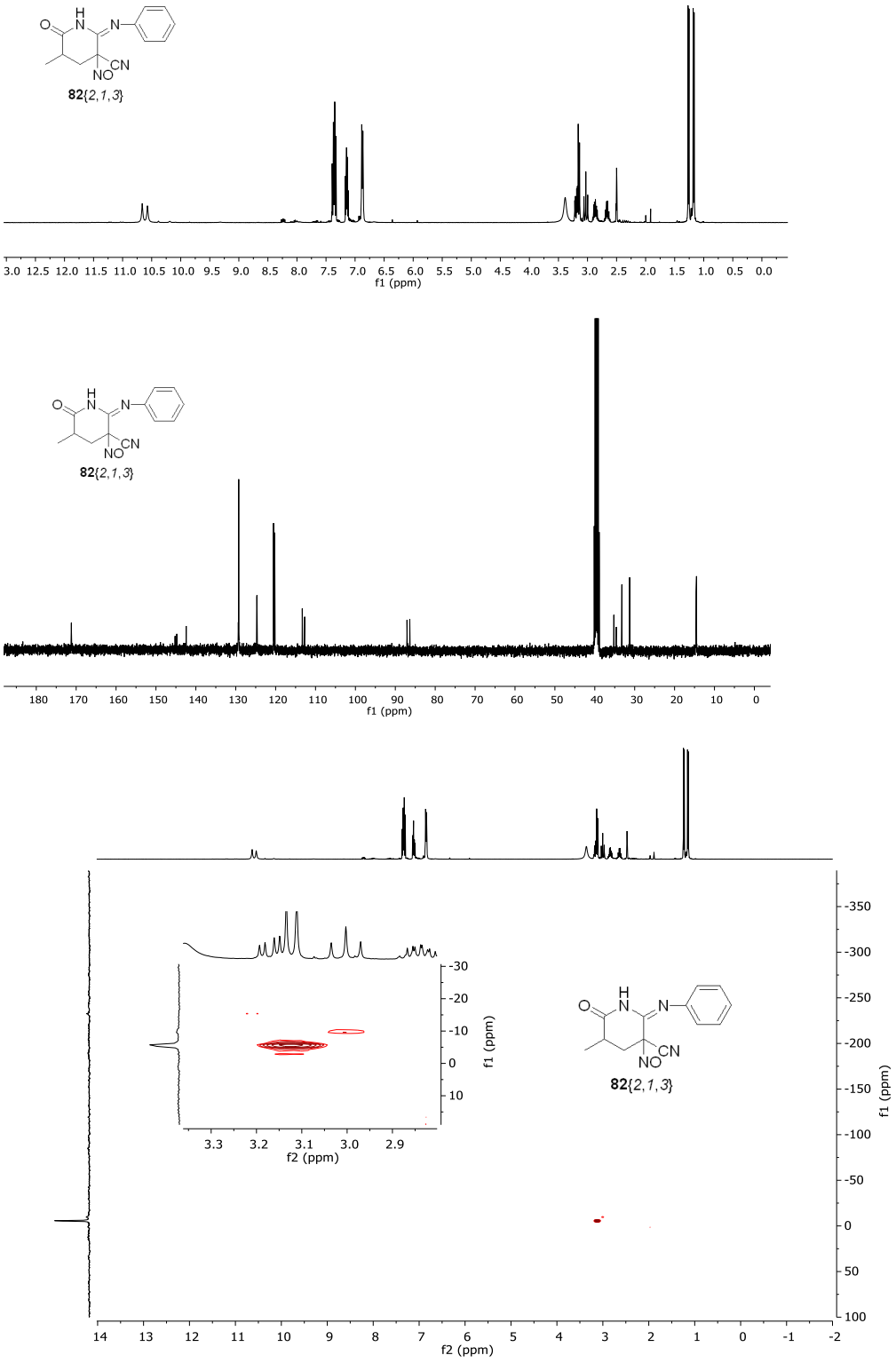

Figure 9.3. Spectroscopy of compound **82**{*2,1,3*}. ^{1}H-NMR, ^{13}C-NMR and ^{15}N-HMBC.

Optimization of the preparation of 5-amino-1-phenyl-1*H*-pyrazole-4-carbaldehyde (92)

Table 9.1. Assays for the complete synthesis of 5-amino-1-phenyl-1H-pyrazolo-4-carbaldehyde (92).

Solvent	Equivalents	Additional equivalents	Temperature / ºC	Time / h	Quenching	Yield / %
Toluene	1:1.1	0	- 78	0.5	H_2SO_4	6.8
Toluene	1:2	0	- 78	18	H_2SO_4	32.0
Toluene	1:2	0	- 78	24	H_2SO_4	31.5
Dichloromethane	1:2	0	- 78	24	H_2SO_4	22.5
Toluene	1:2	0	RT	24	H_2SO_4	53.0
Toluene	1:2	0	RT	24	H_2O	69.1
Toluene	1:2	2	RT	24	H_2O	76.6

Nanoparticles encapsulation

Compound **64**{*7*,*1*,*3*} was encapsulated in PLGA nanoparticles and niosomes at the group of Dr. Manuel Arruebo (Department of Chemical Engineering, Aragon Nanoscience Institute, Zaragoza (Spain)) with the help of Isabel Ortiz de Solorzano and Sara García Salinas. The procedures optimized by this group were applied for the formation of the particles. [1–3]

PLGA nanoparticles

The concentration of compound to perform the encapsulation in PLGA nanoparticles was optimized by preparing 5 batches of nanoparticles with an initial concentration of compound ranging from 1 mg/ml to 0.0625 mg/ml. The amount of compound contained in the nanoparticles was quantified by UV-Vis absorbance (Figure 9.4) after dissolving the particles in AcOEt. The results indicated that it was preferable to work at the lower concentrations (0.0625 (C5) and 0.125 mg/ml (C4)). Particle size was measured using DLS obtaining size values equivalent to the empty nanoparticles (C5 sample = 118 ± 40, C4 sample = 128 ± 37, Empty nanoparticles = 128 ± 41)

The sphere morphology of the particles was observed by scanning electron microscopy (SEM). In the case of the samples prepared with a higher concentration of compound, crystals were observed indicating that the low loading of the particles was caused by the low solubility of the molecule. (Figure 9.5)

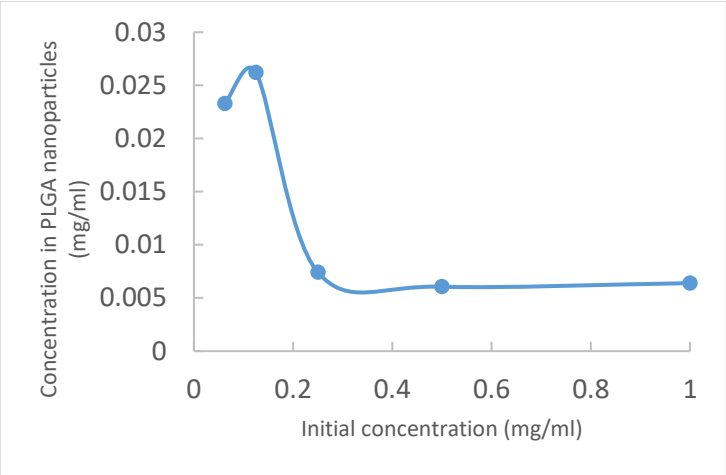

Figure 9.4. Optimization of the initial concentration of compound for the encapsulation in PLGA nanoparticles

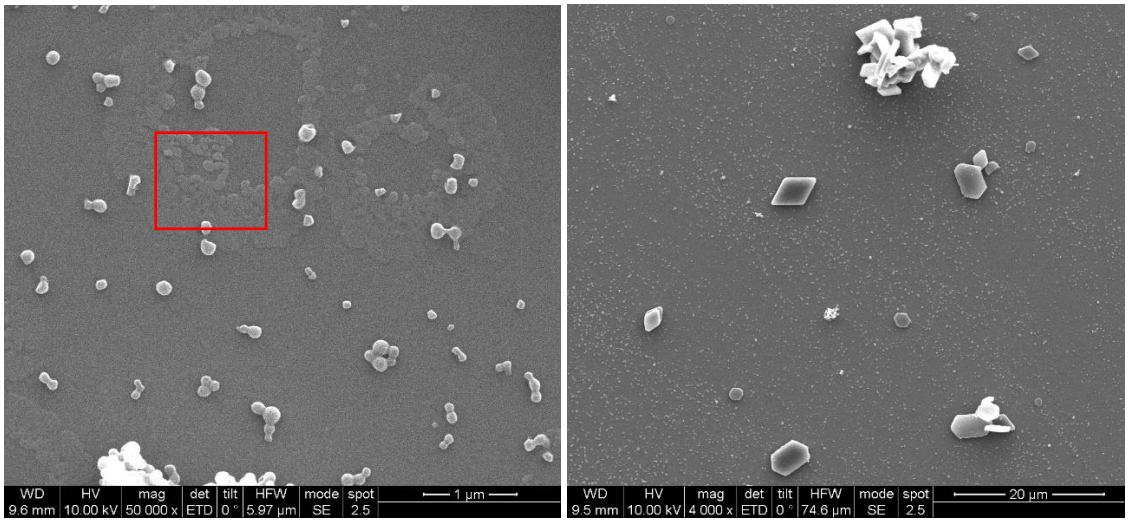

Figure 9.5. SEM images of the encapsulated nanoparticles (A) and the crystals of compounds observed at samples prepared with higher concentrations (B)

Before cell treatment, the amount of encapsulated compound is quantified by HPLC. 0.5 ml of particles suspension are centrifuged (20 min at 13000 rpm) and the pellet is dissolved in CAN (0.5 ml). The samples are quantified by HPLC at the Analytical and applied chemistry of IQS leaded by Dr. Francesc Broto. Method: FM: 45% MeOH – 55% H_2O, Column: C18 encapped 5 µm, Injection volume: 10 µL, Temperature: 40 ºC, Flow rate: 1 ml/min, Detector: UV (270 nm). Sample C4 contained the highest amount of encapsulated compound (12 mg/L) and will be used for cell testing.

Niosome encapsulation

Again, the concentration of compound to perform the encapsulation niosomes was optimized by preparing 5 batches of particles with an initial concentration of compound ranging from 0.5 mg/ml to 0.0375 mg/ml. This time, it was not possible to quantify the amount of encapsulated compound by UV-Vis absorbance as the particles were not soluble in AcOEt Particle size was measured using DLS (C5 sample (initial concentration of 0.0375 mg/ml)= 321 ± 139, Empty nanoparticles = 307 ± 133). Particles prepared with higher concentration present two different populations of niosomes with different sizes (C3 sample (initial concentration of 0.125 mg/ml) = 145 ± 43 and 398 ± 89. The sphere morphology of the particles was observed by transmission electron microscopy (TEM). (Figure 9.6)

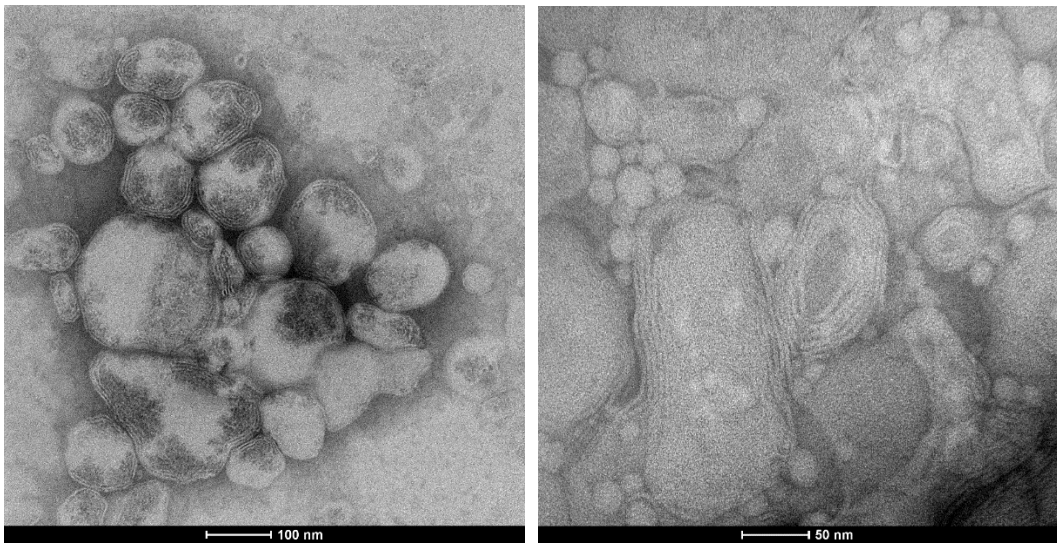

Figure 9.6. TEM images of the niosomes prepared from sample C5 (A) with only one population of niosomes and C3 (B) with two populations with different sizes

The amount of encapsulated compound is quantified by HPLC. 0.5 ml of suspension are mized with 0.5 ml of MeOH, sonicated for 30 minutes and centrifuged (20 min at 13000 rpm). Supernatants are quantified by HPLC at the Analytical and applied chemistry of IQS leaded by Dr. Francesc Broto. Method: FM: 45% MeOH – 55% H_2O, Column: C18 encapped 5 µm, Injection volume: 20 µL, Temperature: 40 ºC, Flow rate: 1 ml/min, Detector: UV (270 nm). Sample C3 contained the highest amount of encapsulated compound (1 mg/L). However, the concentration is too low to use this sample for cell treatment.

Activity study of the encapsulated compound

The effect of the encapsulation was studies by western blot analysis in different cell lines. Compound **64**{*7,1,3*} had not shown any activity alone and the encapsulation was expected to increase the permeability of the compound through the membrane. However, we did not detect inhibition of eIF4E phosphorylation in any of the studies cell lines

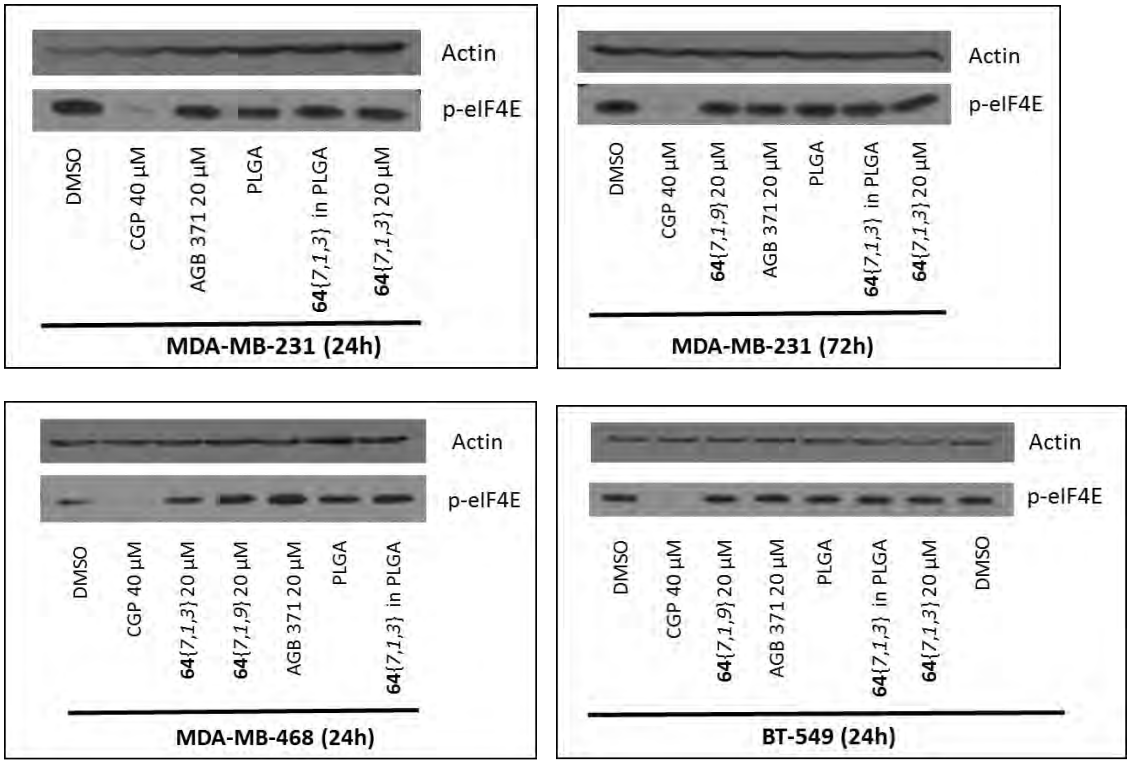

Figure 9.7. Treatment of MDA-MB-231. DA-MB-468 and BT-549 cells with compound **64**{*7,1,3*} encapsulated in PLGA. AGB371 corresponds to a compound from a different project. WB performed after 24h or 72h of treatment. Final DMSO concentration 0.5%. CGP is a known inhibitor used as a positive control.

Effect of compound 106 on other cell lines

Compound **106** was described by Diab *et al.*[33] as a selective inhibitor for AML cells. As expected, the compound inhibits eIF4E phosphorylation in MV4-11 leukemia cells but is not effective on other cell lines (Figure 9.8)

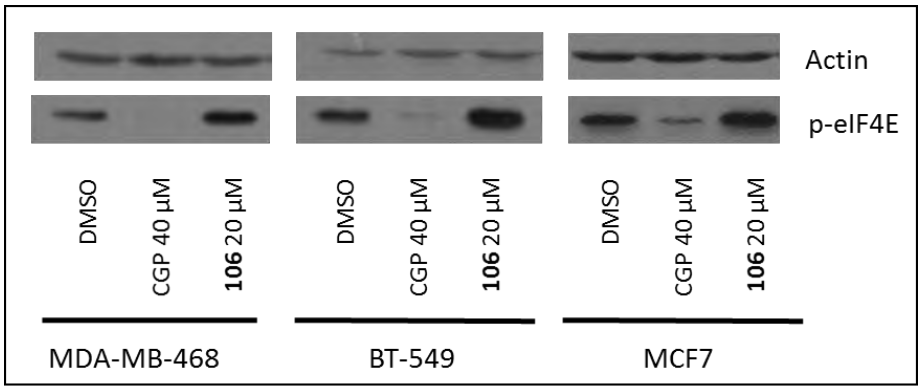

Figure 9.8. Treatment of breast cancer cells with compound **106**. WB performed after 24h of treatment. Final DMSO concentration 0.5%.

Validation of the kinase assays

Some compound showed variable results in the different rounds of testing their effect on the residual activity of MNK1/2. In order to clarify these results, some of the compounds were retested by a second company (Eurofins) with an equivalent test. This time, the results are given as %of inhibition and confirm the inactivity of the tested compounds.

Table 9.2. Results from the enzymatic assay performed by Eurofins ®. Values indicated as % of inhibition of kinases MNK1 and MNK2 after treatment with the indicated compounds at 10 μM.

Compound	MNK1	MNK2
cercosporamide	97	98
CGP57380	88	90
64{*2,1,3*}	7	1
64{*3,1,1*}	8	5
101{*7,1,3*}	6	-6
85{*7,1,3*}	-5	-15
102{*7,1,3*}	5	-3
101{*7,1,2*}	5	-9
85{*7,1,2*}	13	-2
101{*3,1,3*}	10	-8
85{*3,1,3*}	14	10
64{*7,1,3*}	14	4
64{*7,1,2*}	10	4
64{*3,1,3*}	10	10
106	56	86
64{*7,1,4*}	7	1
64{*7,1,10*}	5	11
64{*8,1,3*}	4	-3
64{*7,1,8*}	-6	-8
64{*7,1,9*}	3	-4
64{*6,1,1*}	6	-4
64{*2,1,8*}	-4	-4
64{*5,1,5*}	-3	-4
64{*7,1,5*}	11	35
64{*4,1,4*}	3	-6
76{*7,1,3*}	12	-7
76{*7,1,9*}	12	-6
76{*3,1,9*}	15	-19
64{*3,1,9*}	7	-4
76{*6,1,9*}	14	-3
64{*6,1,9*}	17	-3
76{*7,1,8*}	-18	-3
76{*4,1,9*}	-14	-1
64{*4,1,9*}	-6	4
76{*7,1,5*}	-6	5
64{*7,1,9*}	4	1

ANNEX 3

Study of the benzoylation of 3-amino-pyrazolo[3,4-*b*]pyridin-6-ones

Table 9.3. Proportions of the different compounds A and B depending on the reaction temperature.

Temperature (°C)	Conditions	%B	%A
25	THF (room temperature)	18.7	81.3
40	THF	24.2	75.8
60	Dioxane (MW, 30 min)	33.3	66.7
80	Dioxane (MW, 30 min)	35.1	64.9
100	Dioxane (MW, 30 min)	41.5	58.5
120	Dioxane (MW, 30 min)	51.3	48.7
140	Dioxane (MW, 30 min)	64.1	35.9
160	Dioxane (MW, 30 min)	82.6	17.4
180	Dioxane (MW, 30 min)	86.2	13.8
190	Dioxane (MW, 30 min)	87.0	13.0
200	Dioxane (MW, 30 min)	85.5	14.5

ANNEX 4

Biological studies of compound 127

Preliminary results had shown that compound **127** reduced the phosphorylation of eIF4E in MV4-11 cells. For this reason, this compound was further characterized in other cell lines during a predoctoral research stay at the Lady Davis Institute (Department of Oncology, McGill University).

The effect of the compound on cell growth and protein expression was studied in four different cell lines: a breast cancer cell line (MDA-MB-231), two melanoma cell lines (A375M and MeWo) and an ovarian cell line (A2780). The compound presented a high cytotoxicity at 20 µM as can be seen in the growth curves (Table 9.4) and the analysis of apoptosis (Figure **9.9**). Moreover, compound **127** seems to alter the levels of some proteins related to the eIF4E phosphorylation pathway such as MNK1, 4EBP1 and p-AKT (Figure 9.10).

Table 9.4. Growth curves of MDA-MB-231, A2780, MeWo and A375M cells treated with compound **127**

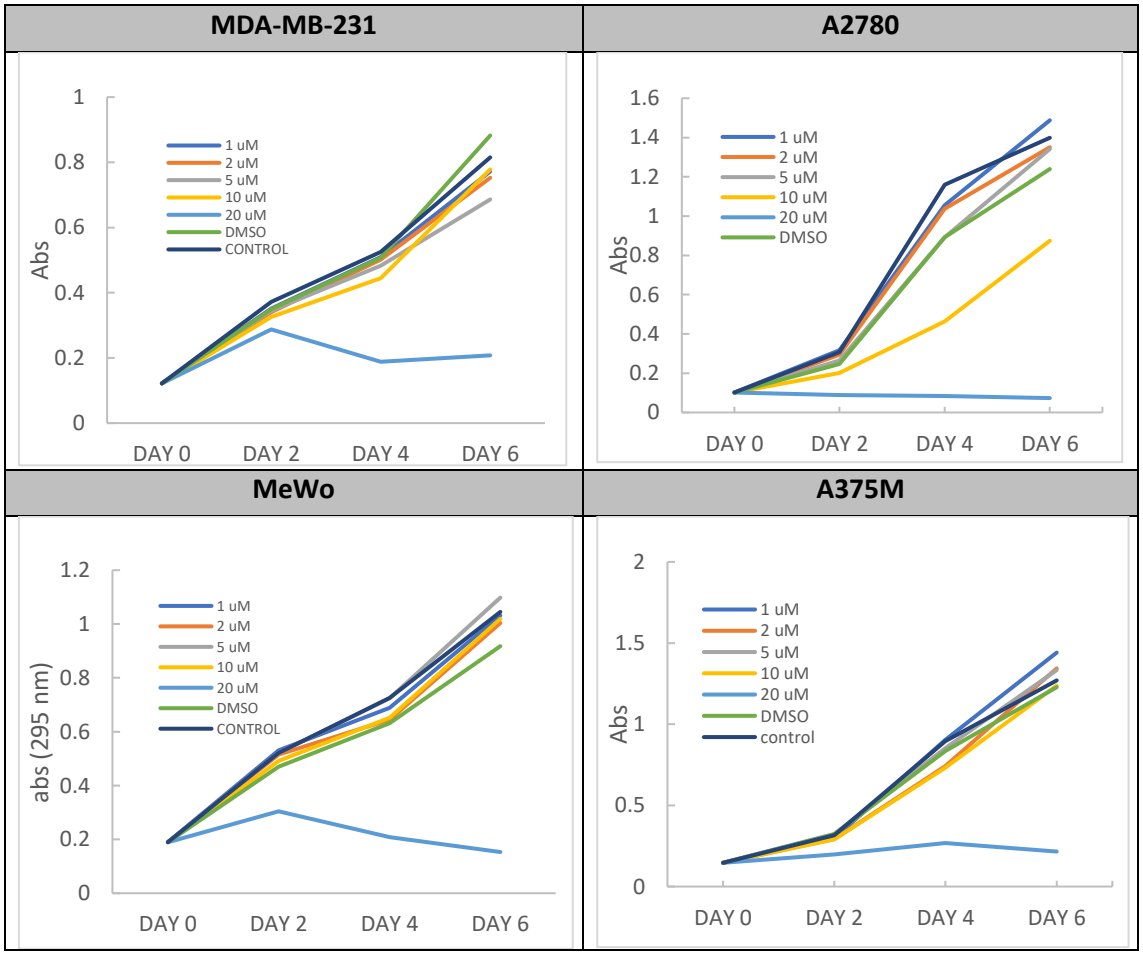

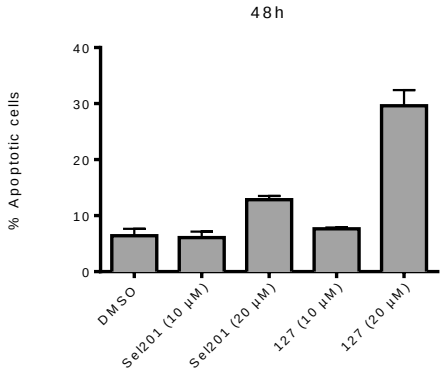

Figure 9.9. Cell death of A375M cells was analyzed by Flow cytometry (Anexin V / PI staining) indicating that compound 127 induces apoptosis at 20 µM

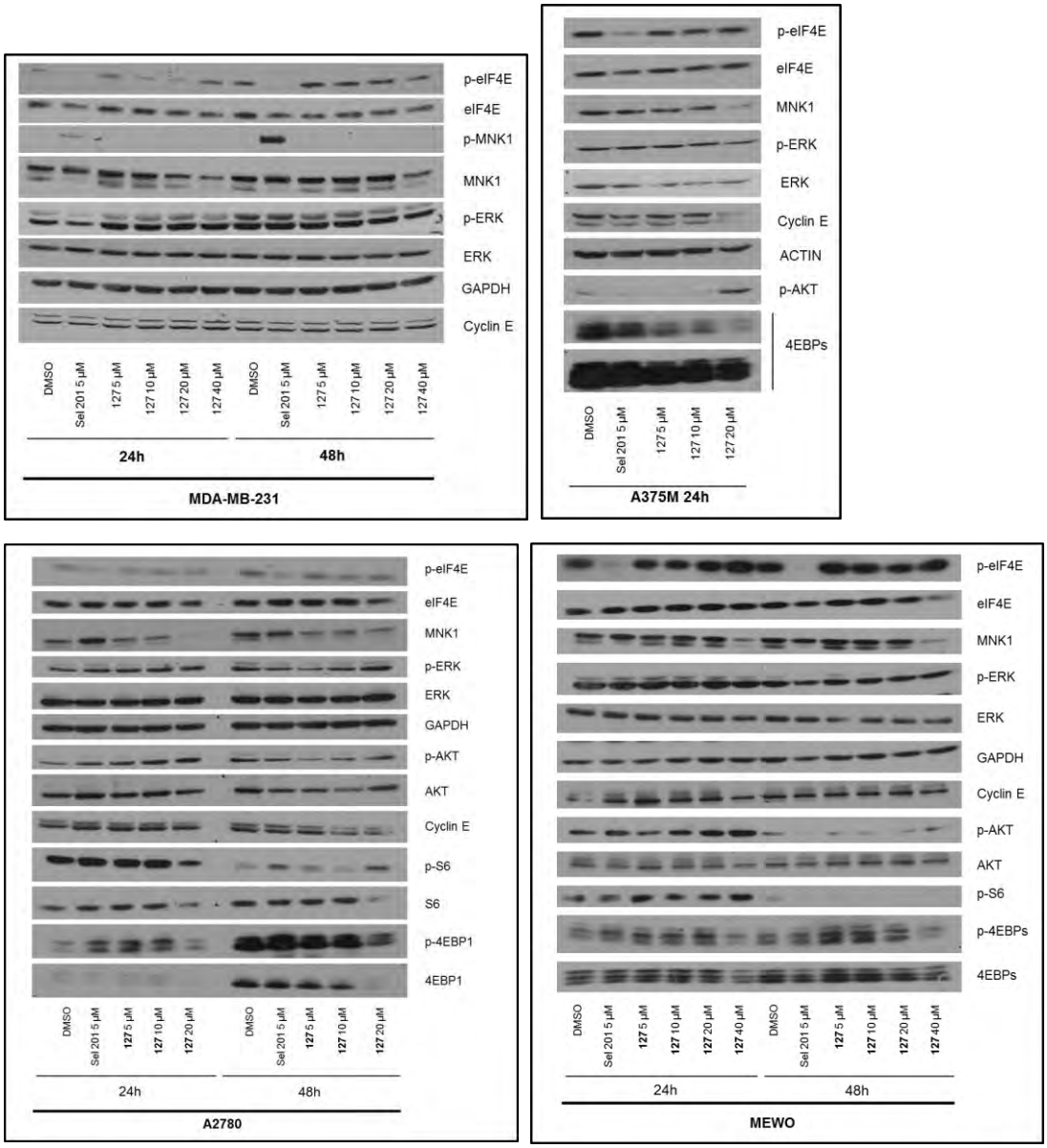

Figure 9.10. Analysis of some proteins involved in the eIF4E phosphorylation pathway that could be affected by the compound.

EB1 titration curves at 24h and 48h in MDA-MB.231 cells

EB1 was shown to reduce eIF4E phosphorylation at 2.5 µM. In Figure 4.34 the inhibition at 72h was shown. Figure 9.11 shows the equivalent studies at 24h and 48h.

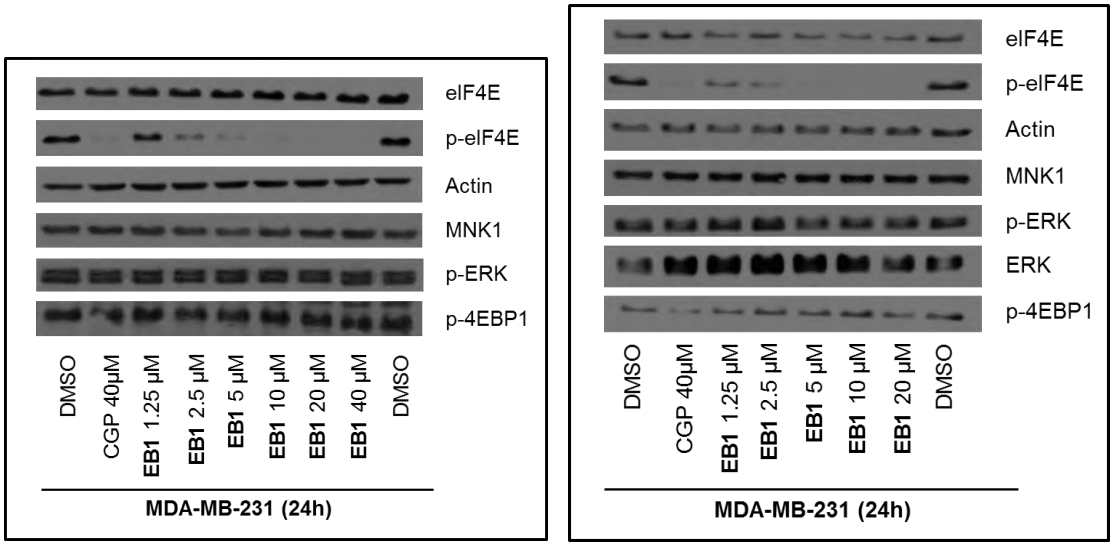

Figure 9.11. Analysis of MDA-MB-231 cells treated with **EB1** for 24h and 48h

EB1 kinome analysis

EB1 was tested in a panel of 320 kinases at 0.1 and 1 µM concentrations. The residual activities measured for each kinase are summarized in the following table.

Table 9.5. Residual activity of a panel of 320 treated with EB1 (0.1 and 1 µM). See page 491.

Kinase Name	1.0E-07	1.0E-06
ABL1	93	94
ABL2	104	81
ACK1	107	85
ACV-R1	78	27
ACV-R1B	86	72
ACV-R2A	104	95
ACV-R2B	72	28
ACV-RL1	74	28
AKT1 aa106-480	98	92
AKT2 aa107-481	105	95
AKT3 aa106-479	96	84
ALK (GST-HIS-tag)	114	93
AMPK-alpha1 aa1-550	94	84
ARK5	105	91
ASK1	96	104
Aurora-A	93	89
Aurora-B	110	112
Aurora-C	98	96
AXL	105	96
BLK	90	65
BMPR1A	102	69
BMX	102	71
B-RAF	80	79
BRK	88	20
BRSK1	108	103
BRSK2	106	79
BTK	92	83
BUB1B	101	94
CAMK1D	80	75
CAMK2A	97	101
CAMK2B	102	84
CAMK2D	98	86
CAMK2G	112	90
CAMK4	104	102
CAMKK1	106	110
CAMKK2	96	96
CDC42BPA	119	109
CDC42BPB	112	120
CDC7/DBF4	103	97
CDK1/CycA2	109	102
CDK1/CycB1	98	90
CDK1/CycE1	83	87
CDK16/CycY	99	92
CDK19/CycC	88	75
CDK2/CycA2	91	79
CDK2/CycE1	86	72
CDK3/CycC	98	102
CDK3/CycE1	116	108
CDK4/CycD1	107	89
CDK4/CycD3	96	86
CDK5/p25NCK	89	88
CDK5/p35NCK	87	81
CDK6/CycD1	93	94
CDK6/CycD3	107	105
CDK7/CycH/MAT1	122	97
CDK8/CycC	88	70
CDK9/CycK	91	86
CDK9/CycT1	110	92
CHK1	105	104
CHK2	102	98
CK1-alpha1	108	89
CK1-delta	91	56
CK1-epsilon	91	47
CK1-gamma1	109	100
CK1-gamma2	110	99
CK1-gamma3	107	98
CK2-alpha1	112	100
CK2-alpha2	119	92
CLK1	119	110
CLK2	106	97
CLK3	117	82
CLK4	101	103
COT	109	92
CSF1-R	114	102
CSK	85	93
DAPK1	104	99
DAPK2	106	94
DAPK3	104	104
DCAMKL2	95	99
DDR2	93	44
DMPK	101	102
DNA-PK	97	86
DYRK1A	101	105
DYRK1B	95	96
DYRK2	99	104
DYRK3	119	118
DYRK4	106	104
EEF2K	97	103
EGF-R	89	53
EIF2AK2	104	106
EIF2AK3	88	83
EPHA1	89	70
EPHA2	102	104
EPHA3	101	96
EPHA4	118	75
EPHA5	102	95
EPHA6	112	88
EPHA7	98	93
EPHA8	121	113
EPHB1	93	88
EPHB2	78	33
EPHB3	91	41
EPHB4	95	90
ERBB2	107	77
ERBB4	93	88
ERK1	96	83
ERK2	102	88

Kinase Name	1.0E-07	1.0E-06
ERK5	99	81
ERK7	104	99
FAK aa2-1052	113	100
FER	113	78
FES	119	100
FGF-R1	113	91
FGF-R2	102	93
FGF-R3	104	94
FGF-R4	109	98
FGR	100	73
FLT3	100	95
FRK	97	52
FYN	93	51
GRK2	106	110
GRK3	114	114
GRK4	98	90
GRK5	122	105
GRK6	119	115
GRK7	94	80
GSG2	95	91
GSK3-alpha	103	83
GSK3-beta	95	91
HCK	98	98
HIPK1	100	95
HIPK2	98	99
HIPK3	98	98
HIPK4	112	88
HRI	123	103
IGF1-R	113	101
IKK-alpha	137	121
IKK-beta	101	89
IKK-epsilon	115	120
INS-R	113	114
INSR-R	91	102
IRAK1	114	96
IRAK4 (untagged)	115	105
ITK	101	106
JAK1 aa583-1154 wt	122	120
JAK2	103	89
JAK3	111	99
JNK1	113	97
JNK2	82	87
JNK3	74	86
KIT	144	106
LCK	98	75
LIMK1	104	89
LIMK2	99	83
LRRK2	108	85
LTK	88	86
LYN	97	81
MAP3K1	105	102
MAP3K10	129	90
MAP3K11	91	52
MAP3K7/MAP3K7IP1	114	105
MAP3K9	106	79
MAP4K2	93	86
MAP4K4	109	90
MAP4K5	98	70
MAPKAPK2	123	97
MAPKAPK3	102	86
MAPKAPK5	108	102
MARK1	99	92
MARK2	104	103
MARK3	107	102
MARK4	108	77
MATK	107	100
MEK1	105	77
MEK2	115	97
MEK5	100	88
MEKK2	113	111
MEKK3	97	94
MELK	102	86
MERTK	102	88
MET	112	104
MINK1	96	91
MKK4	92	100
MKK6 S207D/T211D**	98	90
MKK7	71	71
MKNK1	116	46
MKNK2	117	77
MLK4	79	60
MST1	91	88
MST2	118	105
MST3	118	113
MST4	89	95
mTOR	96	99
MUSK	99	87
MYLK	86	35
MYLK2	69	18
MYLK3	97	31
NEK1	95	99
NEK11	119	103
NEK2	106	108
NEK3	111	104
NEK4	107	110
NEK6	118	115
NEK7	119	117
NEK9	127	109
NIK	111	93
NLK	101	47
p38-alpha	116	87
p38-beta	76	81
p38-delta	107	98
p38-gamma	92	90
PAK1	93	95
PAK2	99	92

Kinase Name	1.0E-07	1.0E-06
PAK3	91	117
PAK4	88	108
PAK6	102	90
PAK7	106	95
PASK	47	6
PBK	110	109
PDGFR-alpha	97	93
PDGFR-beta	86	80
PDK1	109	90
PHKG1	103	102
PHKG2	107	101
PIM1	90	61
PIM2	104	99
PIM3	98	98
PKA	93	67
PKC-alpha	105	102
PKC-beta1	101	100
PKC-beta2	113	102
PKC-delta	127	126
PKC-epsilon	96	95
PKC-eta	88	65
PKC-gamma	104	92
PKC-iota	117	99
PKC-mu	92	88
PKC-nu	89	91
PKC-theta	113	88
PKC-zeta	106	78
PKMYT1	114	95
PLK1	102	88
PLK3	103	97
PRK1	98	101
PRK2	92	94
PRKD2	102	100
PRKG1	98	49
PRKG2	46	8
PRKX	99	88
PYK2	100	89
RAF1 Y340D/Y341D (untagged)**	82	92
RET	91	58
RIPK2	86	64
RIPK5	103	92
ROCK1	90	83
ROCK2	108	110
RON	98	80
ROS	86	77
RPS6KA1	101	68
RPS6KA2	88	80
RPS6KA3	116	82
RPS6KA4	108	111
RPS6KA5	115	89
RPS6KA6	98	80
S6K	99	88
S6K-beta	108	106
SAK	97	101
SGK1	87	56
SGK2	100	62
SGK3	94	64
SIK1	85	102
SIK2	100	97
SIK3	91	86
SLK	99	84
SNARK	143	129
SNK	113	104
SRC (GST-HIS-tag)	84	61
SRMS	104	103
SRPK1	123	112
SRPK2	102	103
STK17A	111	67
STK23	98	92
STK25	103	108
STK33	91	99
STK39	101	100
SYK aa1-635	104	103
TAOK2	103	95
TAOK3	120	110
TBK1	116	108
TEC	98	95
TGFB-R1	142	117
TGFB-R2	111	87
TIE2	104	92
TLK1	104	91
TLK2	113	89
TNK1	99	50
TRK-A	89	49
TRK-B	105	72
TRK-C	104	78
TSF1	112	84
TSK2	111	104
TSSK1	100	87
TTBK1	96	97
TTBK2	103	94
TTK	98	96
TXK	92	50
TYK2	107	94
TYRO3	107	95
VEGF-R1	94	90
VEGF-R2	99	81
VEGF-R3	101	84
VRK1	102	94
VRK2	121	119
WEE1	103	85
WNK1	106	93
WNK2	95	92
WNK3	112	96
YES	99	76
ZAK	98	73
ZAP70	99	97

ANNEX 5

Parameters and results of the QSPR classificatory models

Table 9.6. Parameters and results of the tests of the Mnk1 QSPR classificatory models

	PARAMETERS										RESULTS									
											TRAINING					TEST				
MODEL	INPUT	HIDDEN	NEURONS		OUTPUT	TRAINING CYCLES	LEARNING RATE	%TRAINING	TRAINING	%TEST	TEST	ACCURACY %	PRED1TRUE1	PRED1TRUE0	PRED0TRUE1	PRED0TRUE0	ACCURACY %	PRED1TRUE1	PRED1TRUE0	PRED0TRUE1	PRED0TRUE0
QSPR_MNK1_1	7	2	4	6	2	10000	0.5	80	183	20	46	88.5	58	7	14	104	76.1	13	6	5	22
QSPR_MNK1_2	7	2	4	6	2	20000	0.5	80	183	20	46	88.5	51	0	21	111	80.4	13	4	5	24
QSPR_MNK1_3	7	2	4	6	2	30000	0.5	80	183	20	46	88.5	51	0	21	111	80.4	13	4	5	24
QSPR_MNK1_4	7	2	4	6	2	15000	0.5	80	183	20	46	88.5	51	0	21	111	80.4	13	4	5	24
QSPR_MNK1_5	7	2	4	6	2	10000	0.1	80	183	20	46	86.3	56	9	16	102	76.1	13	6	5	22
QSPR_MNK1_6	7	2	4	6	2	10000	0.5	70	160	30	69	90.6	51	3	12	94	85.5	19	2	8	40
QSPR_MNK1_7	7	2	4	6	2	20000	0.5	70	160	30	69	87.5	47	4	16	93	84.1	21	5	6	37
QSPR_MNK1_8	7	2	4	6	2	2000	0.5	80	183	20	46	88.5	53	2	19	109	82.6	11	1	7	27
QSPR_MNK1_9	7	2	4	6	2	20000	0.1	75	172	25	57	95.4	63	3	5	101	80.7	15	4	7	31
QSPR_MNK1_10	7	2	4	6	2	25000	0.1	75	172	25	57	95.4	63	3	5	101	52.5	16	4	6	31
QSPR_MNK1_11	7	2	4	6	2	15000	0.05	80	183	20	46	94.5	66	4	6	107	84.8	13	2	5	26
QSPR_MNK1_12	7	2	4	6	2	15000	0.05	80	198	20	50	90.9	67	13	5	113	64.0	11	11	7	21
QSPR_MNK1_13	7	2	4	5	2	20000	0.05	80	198	20	50	89.4	66	15	6	111	64.0	10	10	8	22

Table 9.7. Parameters and results of the tests of the Mnk2 QSPR classificatory models

												RESULTS											
													TRAINING						TEST				
MODEL	INPUT	HIDDEN	NEURONS		OUTPUT	TRAINING CYCLES	LEARNING RATE	%TRAINING	TRAINING	%TEST	TEST	ACCURACY %	PRED1TRUE1	PRED1TRUE0	PRED0TRUE1	PRED0TRUE0	ACCURACY %	PRED1TRUE1	PRED1TRUE0	PRED0TRUE1	PRED0TRUE0		
QSPR_MNK2_1	7	2	7	5	2	30000	0.5	80	174	20	43	97.1	70	1	4	99	83.7	17	6	1	19		
QSPR_MNK2_2	7	2	7	4	2	30000	0.3	70	152	30	65	99.3	64	1	0	87	83.1	26	9	2	28		
QSPR_MNK2_3	7	2	7	4	2	10000	0.1	80	174	20	43	96.6	72	4	2	96	88.4	18	5	0	20		
QSPR_MNK2_4	7	2	7	4	2	20000	0.05	80	174	20	43	98.3	72	1	2	99	86.1	18	6	0	19		
QSPR_MNK2_5	7	2	7	4	2	20000	0.04	80	174	20	43	98.3	72	1	2	99	88.4	16	3	2	22		
QSPR_MNK2_6	7	2	7	4	2	15000	0.04	80	174	20	43	98.3	72	1	2	99	88.4	16	3	2	22		

Full factorial design for QSAR Mnk1

This Annex includes the results of the design of experiments carried out for the creation of the QSAR predictive model for Mnk1. A 3^2 full factorial design (two variables with three different levels each). (Table 9.8). Table 9.9 summarizes the results of the different experiences.

Table 9.8 Level values for each variable

VARIABLE	LEVEL		
	1	2	3
(A) Iterations	30000	40000	50000
(B) Learn. rate	0.00001	0.0001	0.001

Table 9.9. Results of each experience

EXPERIENCE	VARIABLE A	VARIABLE B	R^2 TRAININNG
1	1	1	0.41
2	1	2	0.87
3	1	3	0.93
4	2	1	0.41
5	2	2	0.87
6	2	3	0.90
7	3	1	0.39
8	3	2	0.89
9	3	3	0.98

The results of the study are described in Table 9.10, where it can be seen that the contribution of the learning rate (variable B) is much higher than the one of the iterations number (variable A) or the effect of changing both variables at the same time (AB). Figure 9.12 represents of the factorial plot of both variables.

Table 9.10. Analysis of variance

	A	B	AB
SC	0.001	0.514	0.003
Degrees of freedom	2	2	4
CM	0.001	0.257	0.001
Contribution	0.2	99.5	0.3

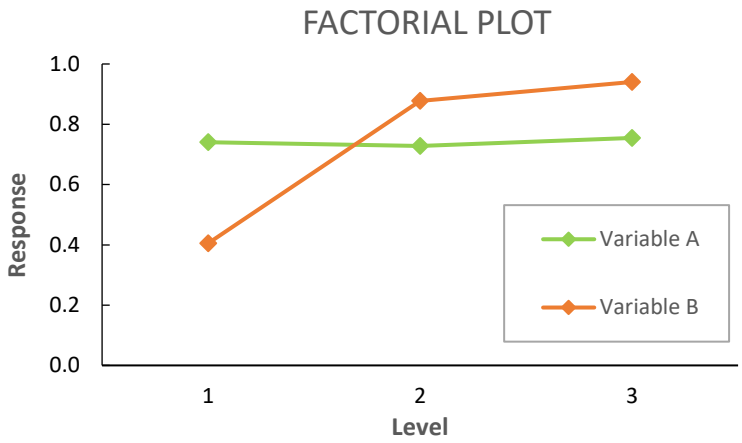

Figure 9.12. Factorial plot obtained for the number of iterations (variable A) and the learning rate (variable B) indicating that the highest response (model accuracy) is obtained with a higher learning rate.

Parameters and results of the QSAR models

In the following figures the results of the QSAR models are summarized. For each model, the input to run the calculation on Aris, the optimization of the parameters and the validation of the methods are included

MNK1 QSAR model

ArIS input of QSAR_MNK1_6_2

```
#Inputs: 7
#Hidden: 2   neurons*: 6 4
#Output: 1

#Iddle: 30000
#ActivFunction: 2
#Learn Rate: 0.0001
#Method: Classification [ ]     |       Prediction [x]

#Class: 1
#OutNumber: 1
#Trainset: 67

#Validation method: 1
#Validation_set: 13

#Testset: 67

#Scale Input Values          [x]
#Test_weight matrix          [x]        name: auto
#Test_architecture           [x]        name: auto
#Inhibit convergence stop    [x]
```

Table 9.11. Parameters and results of the tests of the Mnk1 QSAR classificatory models

MODEL	PARAMETERS							RESULTS					
								TRAINING			TEST		
	REPETITIONS	REPETITION	INPUT	HIDDEN	NEURONS	OUTPUT	IDDLE	LEARN RATE	R^2	RMSE	SPEARMAN	R^2	RMSE	SPEARMAN
QSAR_MNK1_1	1	1	7	2	6	1	5000	0.0001	0.42	0.00	1.00	0.41	0.09	0.98
QSAR_MNK1_2	1	1	7	2	4	1	10000	0.0001	0.60	0.00	1.00	0.44	0.07	0.98
QSAR_MNK1_3	5	1	7	2	6	1	50000	0.0001	0.89	0.00	1.00	0.12	1.18	0.95
		2							0.93	0.00	1.00	0.11	0.37	0.94
		3							0.82	0.00	1.00	0.28	0.86	0.95
		4							0.94	0.00	1.00	0.31	1.56	0.95
		5							0.90	0.00	1.00	0.00	1.73	0.94
QSAR_MNK1_4	1	1	7	2	6	1	30000	0.001	0.93	0.14	1.00	0.22	0.49	0.97
QSAR_MNK1_5	1	1	7	2	6	1	50000	0.001	0.98	0.38	1.00	0.59	1.12	0.97
QSAR_MNK1_6	5	1	7	2	6	1	30000	0.0001	0.87	0.00	1.00	0.58	0.30	0.98
		2							0.79	0.00	1.00	0.72	0.18	0.99
		3							0.73	0.01	1.00	0.83	0.69	0.99
		4							0.87	0.01	1.00	0.31	0.04	0.97
		5							0.88	0.00	1.00	0.40	0.28	0.97
QSAR_MNK1_7	1	1	7	2	6	1	40000	0.0001	0.87	0.00	1.00	0.58	0.20	0.98
QSAR_MNK1_8	1	1	7	2	6	1	25000	0.0001	0.90	0.01	1.00	0.32	1.02	0.94
QSAR_MNK1_9	1	1	7	2	6	1	30000	0.00001	0.41	0.01	1.00	0.41	0.02	0.98
QSAR_MNK1_10	1	1	7	2	6	1	40000	0.00001	0.41	0.01	1.00	0.47	0.15	0.98
QSAR_MNK1_11	1	1	7	2	6	1	50000	0.00001	0.39	0.01	1.00	0.34	0.10	0.98
QSAR_MNK1_12	1	1	7	2	6	1	75000	0.00001	0.43	0.00	1.00	0.41	0.32	0.98
QSAR_MNK1_13	1	1	7	2	6	1	40000	0.001	0.90	0.50	1.00	0.22	0.41	0.93

Model validation

The QSAR_MNK1_6_2 model was validated with the same database used to build the model (*database_papers_mnk1*, IC_{50}<10 µM) representing the ROCS curve for both the training and the test sets (Figure 9.13 and Figure 9.14) and defining different cutoffs. In the case of the training set, the ideal cutoff is 0.78, with a 92% of TPR and 13% of FPR. In the test set, with the same cutoff the TPR is 80% and the FPR is 13%.

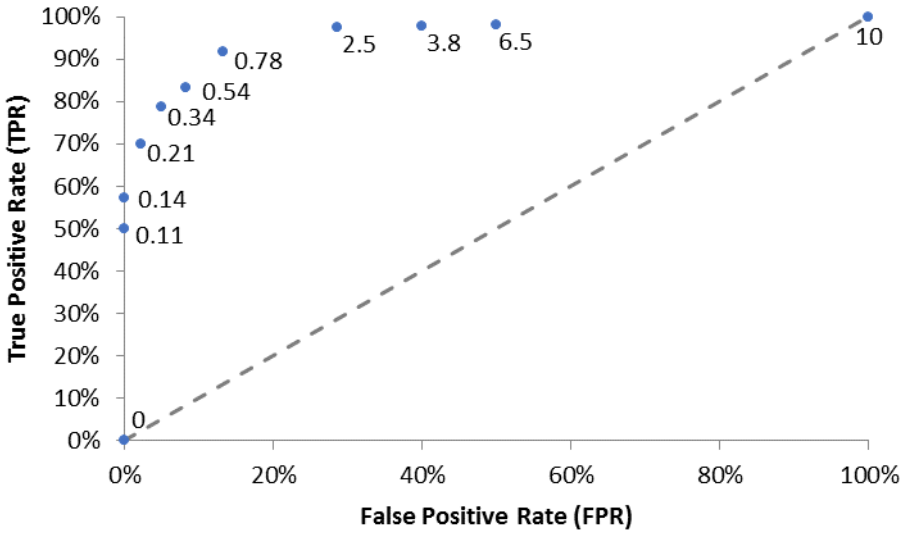

Figure 9.13. ROCS curve for validation of the training set

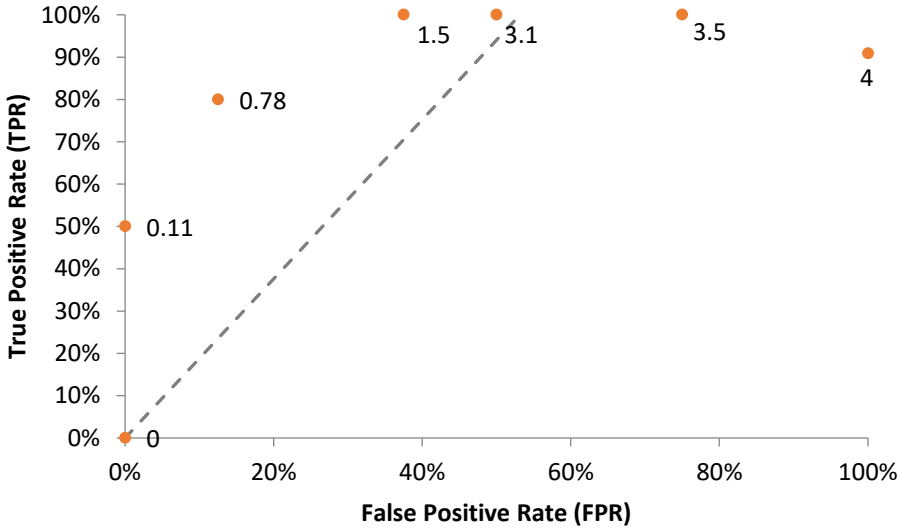

Figure 9.14. ROCS curve for validation of the test set

MNK2 QSAR model

ArIS input of QSAR_MNK2_18_1

```
#Inputs: 5
#Hidden: 2   neurons*: 5 3
#Output: 1

#Iddle: 30000
#ActivFunction: 2
#Learn Rate: 0.001
#Method: Classification [ ]     |       Prediction [x]

#Class: 1
#OutNumber: 1
#Trainset: 47

#Validation method: 1
#Validation_set: 10

#Testset: 47

#Scale Input Values          [x]
#Test_weight matrix          [x]        name: auto
#Test_architecture           [x]        name: auto
#Inhibit convergence stop    [x]
```

Table 9.12. Parameters and results for the test sets of the Mnk2 QSAR classificatory models

	PARAMETERS								RESULTS					
									TRAINING			TEST		
MODEL	REPETITIONS	REPETITION	INPUT	HIDDEN	NEURONS	OUTPUT	IDDLE	LEARN RATE	R^2	RMSE	SPEARMAN	R^2	RMSE	SPEARMAN
QSAR_MNK2_1	5	1	5	2	4 2	1	50000	0.0001	0.80	0.44	1.00	0.12	0.15	0.94
		2							0.70	0.01	1.00	0.08	0.87	0.92
		3							0.57	0.00	1.00	0.00	0.67	0.91
		4							0.53	0.01	1.00	0.16	0.24	0.95
		5							0.65	0.36	1.00	0.16	0.34	0.95
QSAR_MNK2_2	1	1	5	2	4 2	1	30000	0.0001	0.79	0.01	1.00	0.09	0.33	0.92
QSAR_MNK2_3	1	1	5	1	3	1	50000	0.0001	0.51	0.05	1.00	0.15	1.64	0.87
QSAR_MNK2_4	1	1	5	2	4 2	1	50000	0.001	0.91	0.02	1.00	0.24	1.83	0.92
QSAR_MNK2_5	1	1	5	2	4 2	1	50000	0.00001	0.21	0.00	1.00	0.04	0.35	0.94
QSAR_MNK2_6	1	1	5	2	4 2	1	75000	0.00001	0.21	0.02	1.00	0.09	0.26	0.95
QSAR_MNK2_7	5	1	5	2	4 3	1	75000	0.00001	0.21	0.01	1.00	0.06	0.38	0.94
		2							0.25	0.01	1.00	0.03	0.36	0.94
		3							0.22	0.00	1.00	0.08	0.38	0.94
		4							0.23	0.00	1.00	0.11	0.36	0.95
		5							0.21	0.00	1.00	0.10	0.32	0.95
QSAR_MNK2_8	1	1	5	2	4 3	1	75000	0.001	0.98	0.68	1.00	0.09	1.80	0.88
QSAR_MNK2_9	1	1	5	2	4 3	1	50000	0.001	0.94	0.00	1.00	0.01	0.95	0.84
QSAR_MNK2_10	5	1	5	2	4 3	1	30000	0.001	0.80	0.05	1.00	0.38	0.19	0.92
		2							0.75	0.63	1.00	0.05	0.43	0.93
		3							0.84	0.00	1.00	0.05	1.71	0.89
		4							0.89	0.00	1.00	0.12	0.34	0.89
		5							0.83	0.02	1.00	0.09	0.70	0.91
QSAR_MNK2_11	1	1	5	2	4 3	1	30000	0.0001	0.62	0.00	1.00	0.00	0.17	0.90
QSAR_MNK2_12	5	1	5	2	4 3	1	30000	0.0005	0.89	0.03	1.00	0.04	0.32	0.90
		2							0.98	0.00	1.00	0.00	0.90	0.78
		3							0.67	0.00	1.00	0.03	2.25	0.82
		4							0.95	0.00	1.00	0.00	3.52	0.64
		5							0.79	0.49	1.00	0.02	0.06	0.92
QSAR_MNK2_13	1	1	5	2	4 3	1	40000	0.0005	0.70	0.00	1.00	0.07	0.16	0.91
QSAR_MNK2_14	1	1	5	2	4 3	1	30000	0.0007	0.93	0.07	1.00	0.01	0.12	0.87
QSAR_MNK2_15	5	1	5	2	4 3	1	30000	0.0006	0.78	0.00	1.00	0.07	0.62	0.94
		2							0.75	0.00	1.00	0.43	0.22	0.97
		3							0.71	0.35	1.00	0.12	0.41	0.94
		4							0.66	0.02	1.00	0.13	0.96	0.93
		5							0.97	0.01	1.00	0.03	1.20	0.86
QSAR_MNK2_16	1	1	5	2	4 3	1	25000	0.0005	0.88	0.00	1.00	0.28	0.09	0.94
QSAR_MNK2_17	1	1	5	2	4 3	1	28000	0.0005	0.69	0.02	1.00	0.05	0.29	0.93
QSAR_MNK2_18	5	1	5	2	5 3	1	30000	0.001	0.81	0.02	1.00	0.28	0.48	0.95
		2							0.86	0.38	1.00	0.10	0.28	0.95
		3							0.99	0.00	1.00	0.43	0.28	0.95
		4							0.94	0.00	1.00	0.08	1.27	0.92
		5							0.89	0.20	1.00	0.11	1.35	0.91

Study of outliers in the MNK2 QSAR model

Model QSAR_MNK2_18_1 was studied for the presence of outliers as the visual inspection of the prediction of the test set indicated a good correlation that was not supported by the statistical analysis (R^2 of 0.28). Molecule 141 was identified as a possible outlier as it was predicted with a much better activity than the real one.

The representation of the confidence interval of 95% confirmed that the compound was an outlier. As this molecule was part of the test set, it was removed to recalculate the accuracy of the model.

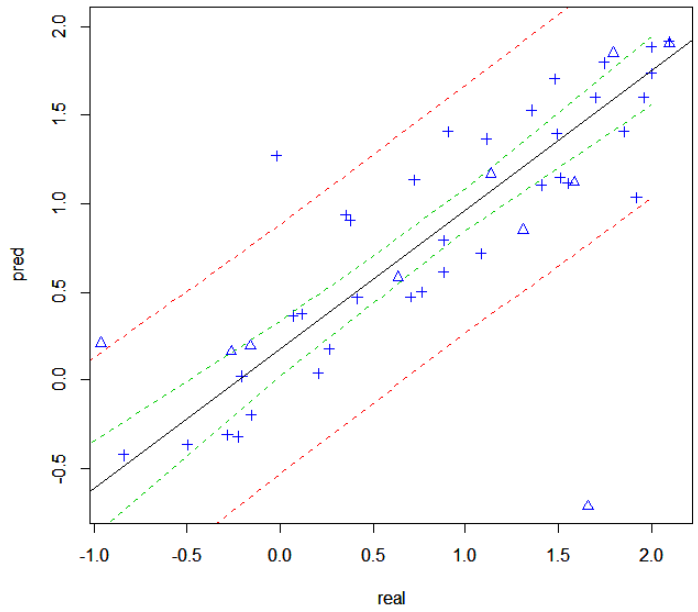

Figure 9.15. Confidence interval of 95% (dashed lines in red) of the QSAR_MNK2_18_1

Model validation

The model was validated with the same database used to build the model (*database_papers_mnk2*, IC_{50}<10 µM) plotting the ROCS curve for both the training and the test sets, defining different cutoffs (Figure 9.16 and Figure 9.17). The ideal cutoff of the training set is 0.09, with a 88% of TPR and 14% of FPR. In the test set, with the same cutoff the TPR is 80% and the FPR is 0%.

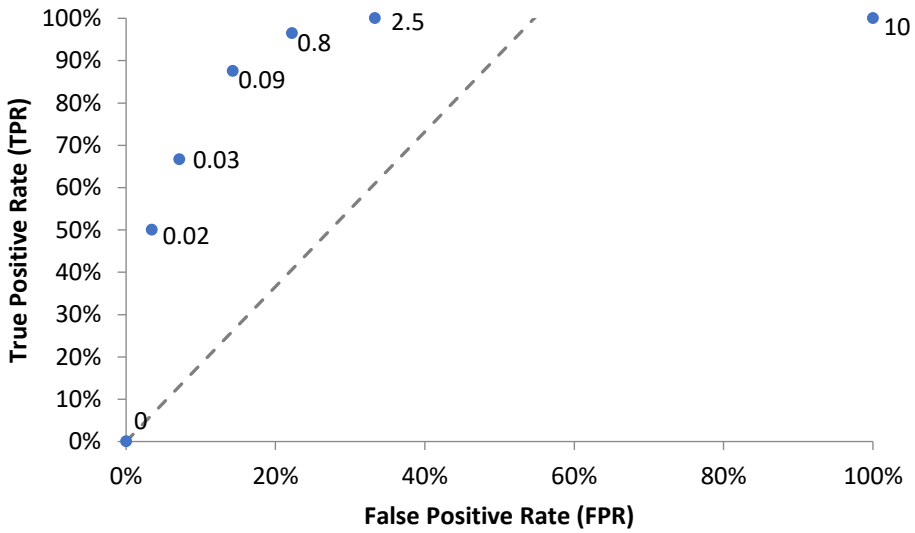

Figure 9.16. ROCS curve for validation of the training set

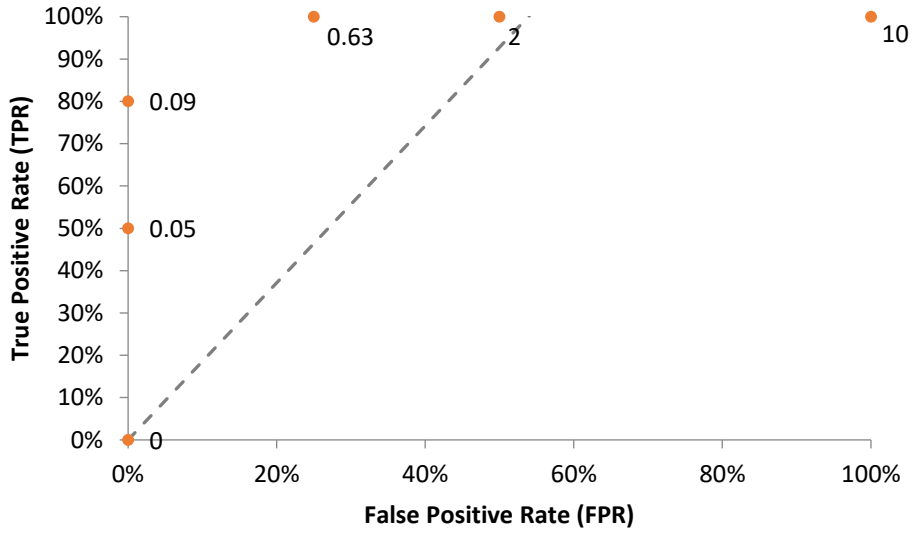

Figure 9.17. ROCS curve for validation of the test set

Study of the suitability of the model

Table 9.13. Prediction of the activity values of the new published inhibitors. Active molecules are marked in blue (MNK1 inhibition) and green (MNK2 inhibition).

ARTICLE	Activity (IC_{50})		Prediction	
	MNK1	MNK2	MNK1	MNK2
Diab2016_6a	49	50	0	0
Diab2016_6b	77	50	0	0
Diab2016_6c	48	46	0	0
Diab2016_6d	57	79	0	0
Diab2016_6e	100	101	0	0
Diab2016_6f	57	68	0	0
Diab2016_6g	68	72	0	0
Diab2016_6h	91	87	0	0
Diab2016_6i	25	68	1	0
Diab2016_6j	102	74	0	0
Diab2016_6k	57	73	0	0
Diab2016_6l	46	53	1	0
Diab2016_10a	44	44	0	0
Diab2016_10b	73	38	0	0
Diab2016_10c	64	48	1	0
Diab2016_10d	26	13	0	0
Diab2016_10e	97	75	0	0
Diab2016_12b	25	17	0	1
Diab2016_12c	88	84	0	0
Diab2016_12a	13	21	0	1
Diab2016_16a	10	8	1	1
Diab2016_16b	63	48	0	1
CGP57380	19	1	1	1

ARTICLE	Activity (IC_{50})		Prediction	
	MNK1	MNK2	MNK1	MNK2
Han2016_2	0.7	0.9	0	0
Han2016_3	0.12	0.72	0	0
Han2016_4	0.036	0.034	0	0
Han2016_5	0.004	0.002	0	0
Han2016_6	0.08	0.02	0	0
Han2016_7	0.002	0.001	0	0
Han2016_8	0.0015	0.0007	0	0
Han2016_9	0.003	0.003	0	0
Zhan2017 (Sel201)	0.0108	0.0054	0	0
Reich2018_1	0.06		1	1
Reich_2	1.8		0	0
Reich_4	6.4		0	1
Reich_3	3.8		0	0
Reich_5	4.7		0	0
Reich_6	5.5		0	0
Reich_7	0.69		0	1
Reich_9	0.023		1	1
Reich_9	0.028	0.045	1	1
Reich_10	0.1	0.061	0	1
Reich_11	3		0	1
Reich_12	0.06	0.057	0	1
Reich_13	0.0065	0.0026	0	1
Reich_14	0.01	0.019	0	1
Reich_15	0.0033	0.0012	0	1
Reich_16	0.0019	0.0057	0	1
Reich_21	0.00065	0.00068	0	0
Reich_22		0.00036	0	0
Reich_20	0.00051	0.0018	1	1
Reich_17	0.0027	0.0023	0	1
Reich_18	0.0016	0.0012	0	0
Reich_19	0.0015	0.0078	0	0
Reich_23	0.0024	0.001	0	0
Reich_24	0.0022	0.00014	0	0
Reich_25	0.00088	0.00013	0	0
Reich_26	0.0014	0.001	0	0
Teo2016_MNKI-19	0.186	0.068	1	1
Teo2015_MNKI-85		0.031	0	1

Validation of the final model.

Table 9.14. Prediction of the activity of pyrazolopyridin-6-ones and pyrazolo[3,4-b]pyridine-3-amino

ID	MNK1	PRED MNK1	MNK2	PRED MNK2
Cercosporamide	0	5.00	1.0	1.00
CGP57380	25	5.00	59.0	4.00
64{*2,1,3*}	145	0.00	112.0	0.00
64{*3,1,1*}	133	0.00	134.0	0.00
101{*7,1,3*}	100	0.00	113.0	3.00
85{*7,1,3*}	142	0.00	99.0	0.00
102{*7,1,3*}	12	0.00	7.0	0.00
101{*7,1,2*}	8	0.00	108.0	0.00
85{*7,1,2*}	133	0.00	27.0	1.00
101{*3,1,3*}	150	0.00	112.0	0.00
85{*3,1,3*}	136	0.00	131.0	0.00
64{*2,1,1*}	145	0.00	97.0	0.00
64{*2,1,2*}	113	0.00	123.0	0.00
64{*7,1,3*}	150	1.00	125.0	4.00
64{*7,1,2*}	8	0.00	4.0	0.00
64{*3,1,3*}	135	0.00	110.0	0.00
64{*2,1,3*}	133	0.00	74.0	0.00
106	55	1.00	42.0	3.00
64{*7,1,4*}	131	0.00	109.0	0.00
64{*7,1,10*}	103	0.00	70.0	0.00
64{*8,1,3*}	144	0.00	101.0	0.00
64{*7,1,8*}	84	0.00	68.0	0.00
64{*6,1,1*}	88	0.00	103.0	0.00
64{*4,1,1*}	105	0.00	107.0	0.00
64{*5,1,1*}	88	1.00	97.0	0.00
64{*1,3,2*}	90	0.00	92.0	0.00
64{*1,3,1*}	93	0.00	90.0	0.00
64{*1,3,3*}	89	0.00	98.0	0.00
64{*2,1,8*}	88	0.00	85.0	0.00
64{*5,1,5*}	111	0.00	73.0	0.00
64{*8,1,1*}	88	0.00	95.0	0.00
64{*5,1,3*}	105	0.00	108.0	0.00
64{*7,1,3*}	92	0.00	97.0	0.00
64{*5,1,6*}	90	0.00	107.0	0.00
64{*7,1,5*}	117	0.00	64.0	0.00
64{*4,1,4*}	86	0.00	98.0	0.00
64{*1,4,3*}	86	0.00	94.0	0.00
64{*3,1,3*}	95	0.00	108.0	0.00
94	89	1.00	96.0	1.00
100	95	1.00	102.0	0.00

ID	MNK1	PRED MNK1	MNK2	PRED MNK2
96	109	1.00	94.0	0.00
98	99	0.00	105.0	0.00
64{*7,1,1*}	110	0.00	97.0	0.00
64{*7,1,3*}	106	0.00	104.0	0.00
85{*7,1,3*}	115	0.00	103.0	0.00
64{*1,4,9*}	99	0.00	102.0	5.00
123	97	2.00	99.0	0.00
64{*7,1,9*}	91	0.00	97.0	5.00
127	103	3.00	102.0	0.00
126	111	0.00	106.0	1.00
64{*6,1,9*}	106	0.00	95.0	3.00
64{*4,1,9*}	101	0.00	98.0	2.00
64{*1,3,9*}	114	0.00	104.0	4.00
64{*1,4,8*}	96	1.00	99.0	5.00
64{*3,1,9*}	117	0.00	99.0	2.00
134	94	1.00	95.0	0.00
101	91	0.00	111.0	0.00
109{*1,2,3*}	98	2.00	102.0	0.00
109{*1,3,3*}	113	0.00	101.0	2.00
110{*1,2,3*}	103	0.00	101.0	1.00
110{*1,3,3*}	108	0.00	104.0	3.00
110{*2,1,3*}	105	1.00	95.0	1.00
110{*2,1,2*}	102	0.00	99.0	2.00
110{*1,4,2*}	104	1.00	101.0	5.00
110{*1,2,2*}	102	2.00	94.0	1.00
139{*4,4,1*}	60	1.00	101.0	0.00
139{*5,6,1*}	51	4.00	82.0	0.00
139{*3,4,1*}	25	1.00	74.0	0.00
139{*4,5,1*}	45	1.00	82.0	0.00
139{*5,3,1*}	38	1.00	74.0	0.00
139{*5,4,1*}	41	1.00	92.0	0.00
139{*6,4,1*}	63	1.00	109.0	0.00
139{*3,6,1*}	31	5.00	62.0	0.00
139{*6,5,1*}	61	3.00	123.0	0.00
139{*4,4,2*}	94	0.00	154.0	0.00
139{*3,4,2*}	102	0.00	145.0	0.00
139{*3,3,1*}	19	3.00	56.0	0.00
139{*3,3,2*}	80	1.00	117.0	0.00
139{*1,1,2*}	106	0.00	95.0	1.00
139{*1,1,1*}	95	3.00	102.0	1.00

MMPBSA Inputs

Example of MMPBSA input of 2hw6 model with EB1. Extraction of snapshots.

Input based on the inputs generated by Holger Gohlke for the AMBER advanced tutorial 3 (section3)

```
# Input parameters for mm_pbsa.pl
#####################################################################
@GENERAL
#
PREFIX                  snapshot
PATH                    ./extract/
#
COMPLEX                 1
RECEPTOR                1
LIGAND                  1
#
COMPT                   ../top/complex_wat.prmtop
RECPT                   ../top/rec.prmtop
LIGPT                   ../top/lig.prmtop
#
GC                      1
AS                      0
DC                      0
#
MM                      0
GB                      0
PB                      0
MS                      0
NM                      0
#####################################################################
@MAKECRD
#
BOX                     YES
NTOTAL                  49083
NSTART                  22500
NSTOP                   25000
NFREQ                   1
#
NUMBER_LIG_GROUPS       1
LSTART                  4683
LSTOP                   4718
NUMBER_REC_GROUPS       1
RSTART                  1
RSTOP                   4682
#####################################################################
@TRAJECTORY
#
TRAJECTORY              ../mdcrd/md_2hw6_AJL117pos11.mdcrd
@PROGRAMS
```

Example of MMPBSA input of 2hw6 model with EB1. Binding energy

Input based on the inputs generated by Holger Gohlke for the AMBER advanced tutorial 3 (section3)

```
# Input parameters for mm_pbsa.pl
#
#####################################################################
@GENERAL
#
VERBOSE                 0
PARALLEL                0
#
PREFIX                  snapshot
PATH                    ./extract/
START                   12500
STOP                    15000
OFFSET                  1
#
COMPLEX                 1
RECEPTOR                1
LIGAND                  1
#
COMPT                   ../top/complex.prmtop
RECPT                   ../top/rec.prmtop
LIGPT                   ../top/lig.prmtop
#
GC                      0
AS                      0
DC                      0
#
MM                      1
GB                      1
PB                      1
MS                      1
#
NM                      0
#
#####################################################################
@PB
#
PROC                    2
REFE                    0
INDI                    1.0
EXDI                    80.0
SCALE                   2
LINIT                   1000
ISTRNG                  0.0
RADIOPT                 0
ARCRES                  0.0625
INP                     1
#
#
```

```
SURFTEN                 0.005
SURFOFF                 0.00
#
IVCAP                   0
CUTCAP                  -1.0
XCAP                    0.0
YCAP                    0.0
ZCAP                    0.0

#####################################################################
@MM
#
DIELC                   1.0

#####################################################################
@GB
#
IGB                     2
GBSA                    1
SALTCON                 0.00
EXTDIEL                 80.0
INTDIEL                 1.0
#
SURFTEN                 0.005
SURFOFF                 0.00

#####################################################################
@MS
#
PROBE                   0.0
#
@PROGRAMS
#####################################################################
```

CPPTRAJ inputs.

Cluster analysis of 2hw6 model without the loop atoms

```
parm ../../../2hw6_nwi.prmtop

trajin ../../../AMD_2hw6.mdcrd

rms :1-159,186-223,254-299@CA first out rmsd_2hw6_noloop.txt

cluster C0 dbscan minpoints 25 epsilon 0.9 sievetoframe \
rms :1-159,186-223,254-299@CA sieve 10 \
out cnumvtime.dat summary summary.dat info info.dat \
cpopvtime cpopvtime.agr normframe \
repout rep repfmt pdb singlerepout \
singlerep.mdcrd singlerepfmt mdcrd avgout Avg avgfmt restart \
run
```

Intermolecular H-bond analysis

```
parm ../top/complex.prmtop
trajin ../mdcrd/md_2hw6pos11_AJL117_nw.mdcrd

######################################## INTERMOLECULAR HBONDS
hbond AJL117_2hw6pos11 out hbonds/AJL117_2hw6_pos11.dat
acceptormask :300 donormask :1-299 nointramol avgout
hbonds/AJL117_2hw6_pos11.avg.dat
hbond 2hw6_AJL117_pos11 out hbonds/2hw6_AJL117_pos11.dat
acceptormask :1-299 donormask :300 nointramol avgout
hbonds/2hw6_AJL117_pos11.avg.dat
create hbonds/nhbvtime_AJL117_2hw6_pos11.agr
AJL117_2hw6_pos11[UU]
create hbonds/nhbvtime_2hw6_AJL117_pos11.agr
2hw6_AJL117_pos11[UU]
run

########################### GRAPHICAL REPRESENTATIONS
create hbonds/nhbvtime_allintermolecular.agr
AJL117_2hw6_pos11[UU] 2hw6_AJL117_pos11[UU]
run
```

Distance between O of Glu88 and the NH_2 of EB1

```
parm ../top/complex.prmtop
trajin ../mdcrd/md_2hw6pos11_AJL117_nw.mdcrd

distance Glu88_NH2 :88@O :300@H4 out Glu88_NH2.agr noimage
run
```

Publications

ChemPubSoc Europe

DOI: 10.1002/slct.201700732

Chemistry SELECT Full Papers

Organic & Supramolecular Chemistry

An Unequivocal Synthesis of 2-Aryl Substituted 3-Amino-2,4,5,7-tetrahydro-6*H*-pyrazolo[3,4-*b*] pyridin-6-ones

Elisabeth Bou-Petit,[a] Elsa Picas,[a] Cristina Puigjaner,[b] Mercè Font-Bardia,[c] Nabí Ferrer,[a] Julià Sempere,[a] Raimon Puig de la Bellacasa,[a] Xavier Batllori,[a] Jordi Teixidó,[a] Roger Estrada-Tejedor,[a] Santiago Ramon y Cajal,[d] and José I. Borrell*[a]

The reaction between pyridones (**1**) and substituted hydrazines **4** can afford two different regioisomeric pyrazolo[3,4-*b*]pyridin-6-ones **2** and **3** depending on the initial substitution of the methoxy group and the direction of the cyclization. In the case of phenylhydrazine **4** (R^3 = Ph), we have clearly shown that the treatment of pyridones **1a–d** with **4** (R^3 = Ph) in MeOH at temperatures below 140°C yields, independently of the nature and position of the substituents present in the pyridone ring, the open intermediates **7a–d.** When the reaction is carried at 140°C under microwave irradiation, the corresponding 2-aryl substituted pyrazolo[3,4-*b*]pyridines **3a–d** are always formed. We have experimentally determined, using DSC techniques, the activation energies of the two steps involved in the formation of **3:** a) substitution of the methoxy group present in pyridones **1** with phenylhydrazine **4** (R^3 = Ph) to afford intermediates **7** and b) cyclization of intermediates **7** to yield pyrazolopyridines **3.** The results obtained, 15 and 42 kcal·mol^{-1} respectively, are in agreement with the experimental findings.

Introduction

As a part of our ongoing research in the area of tyrosine kinase inhibitors, we were interested in 3-amino-2,4,5,7-tetrahydro-6*H*-pyrazolo[3,4-*b*]pyridin-6-ones[1] as an scaffold for the synthesis of combinatorial libraries. Such structures can be obtained by cyclization of 2-methoxy-6-oxo-1,4,5,6-tetrahydropyridin-3-carbonitriles (**1**), synthesized by reaction of an α,β-unsaturated ester and malononitrile in NaOMe/MeOH,[2] with hydrazine[3] or substituted hydrazines. In this later case, the reaction can lead to two different positional isomers (**2** or **3**) depending on the reaction path. If the substitution of the methoxy group present in **1** takes place with the NH group of the substituted hydrazine the subsequent cyclization onto the cyano group would afford **2** (path A). On the contrary, if the initial attack is carried out by the NH_2 group the cyclization would yield **3** (path B) (Scheme 1).

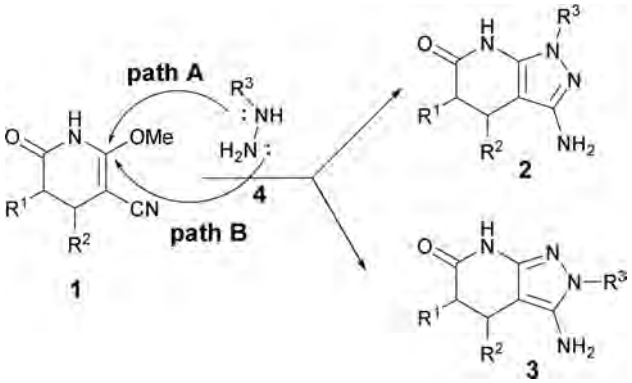

Scheme 1. Possible reaction pathways for the formation of pyrazolo[3,4-*b*] pyridin-6-ones **2** and **3.**

In principle, the initial substitution should be governed by the relative nucleophilicity of the two nitrogen atoms present in NH_2-NH-R^3, provided that the steric effects are negligible. Consequently, if R^3 is a donor group the nucleophilic character of the nitrogen bonded to R^3 should be increased, thus favoring the attack of the NH group, leading to the formation of isomer **2.** On the contrary, if R^3 is an electron-withdrawing

[a] *E. Bou-Petit, E. Picas, N. Ferrer, Prof. J. Sempere, Dr. R. Puig de la Bellacasa, Dr. X. Batllori, Prof. J. Teixidó, Dr. R. Estrada-Tejedor, Prof. J. I. Borrell*
IQS School of Engineering
Universitat Ramon Llull
Via Augusta, 390, E-08017 Barcelona, Spain
E-mail: j.i.borrell@iqs.url.edu
[b] *Dr. C. Puigjaner*
Unitat de Polimorfisme i Calorimetria
Centres Cientificotècnics
Universitat de Barcelona
Baldiri Reixac 10, 08028 Barcelona, Spain
[c] *Dr. M. Font-Bardia*
Unitat de Difracció de Raigs X
Centres Cientificotècnics
Universitat de Barcelona
Lluís Solé i Sabarís 1–3, 08028 Barcelona, Spain
[d] *Prof. S. Ramon y Cajal*
Departamento de Patología
Hospital Universitario Valle de Hebrón
Universidad Autónoma de Barcelona
Passeig Vall d'Hebron 119–129, 08035 Barcelona, Spain

Supporting information for this article is available on the WWW under https://doi.org/10.1002/slct.201700732

group the initial substitution should proceed through the NH_2 nitrogen, thus leading to isomer **3.**

In the case of phenyl substituted hydrazines the prediction[4] of the pKa values indicates that the NH_2 group should be more nucleophilic (pKa = 27.8) in comparison with the NH group (pKa = 21.7). Consequently, it would be reasonable to expect that the reaction could proceed affording isomer **3** as stated above.

According to our design for potential activity as tyrosine kinase inhibitors, we were interested in 2-aryl substituted structures **3.** A literature search revealed that there is not a single example of such kind of structures, and only a work by Rodrigues-Santos *et al.* published in 2011 in which they claimed that the reaction with phenylhydrazine **4** (R^3 = Ph) (or substituted phenylhydrazines) only affords isomer **2.**[5]

Consequently, we decided to revise the reaction between pyridones **1** and phenylhydrazine **4** (R^3 = Ph). The present paper deals with the results obtained in such study.

Results and Discussion

We selected a set of α,β-unsaturated esters **5a–d** to synthesize the corresponding 2-methoxy-6-oxo-1,4,5,6 tetrahydropyridin-3-carbonitriles **1a–d** in 40–78% yield, upon treatment with malononitrile (**6**) in NaOMe/MeOH (Scheme 2), to study the

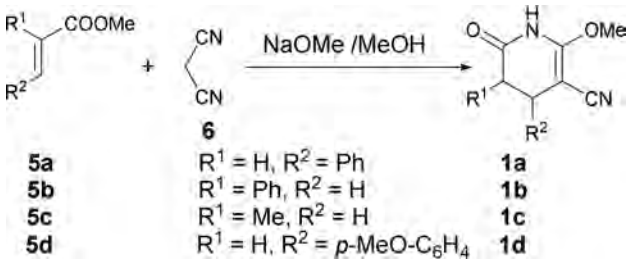

Scheme 2. Synthesis of 2-methoxy-6-oxo-1,4,5,6 tetrahydropyridin-3-carbonitriles **1a–d.**

effect of the substituents R^1 and R^2 in the subsequent reaction with phenylhydrazine **4** (R^3 = Ph).

First, we decided to reproduce the experimental conditions used by Rodrigues-Santos *et al.*[5] using pyridone **1a** and phenylhydrazine **4** (R^3 = Ph). It is necessary to point out that they described that the reaction affords pyrazolopyridines **2** both with conventional heating and microwave irradiation using a domestic microwave oven (2450 MHz). Surprisingly, when we treated **1a** with phenylhydrazine **4** (R^3 = Ph) using the conventional heating methodology (at reflux for 24 h using MeOH as solvent) a product was isolated in 74% yield whose structure was different from **2** or **3.** In particular, the presence in the IR spectrum of a C≡N stretching band at 2256 cm^{-1} revealed that the cyclization was not achieved. Moreover, in the ^{1}H-NMR spectrum the signal corresponding to the methoxy group of **1a** (3.94 ppm) had disappeared, the N–H of the lactam group appeared as a singlet at 10.32 ppm while a second N2-H singlet appeared at 9.11 ppm and a doublet, corresponding to the α-cyano C–H, was observed at 4.69 ppm. These evidences clearly indicate that the isolated product was the reaction intermediate **7a** (R^1 = H, R^2 = Ph) (Figure 1) which had not completed the cyclization.

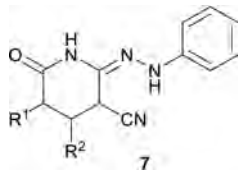

Figure 1. Structure of reaction intermediates **7.**

Our hypothesis was confirmed using NOESY spectroscopy (Figure 2) where the correlation between N1-H/N2-H groups is clearly observed as well as the correlation between H12 of the phenyl group and the N2-H.

Such result led us to study such reaction in deep by using one or two equivalents of phenylhydrazine **4** (R^3 = Ph) in several solvents under different temperature and time conditions. Moreover, two different work-up methods were tested (i.e. filtration and CH_2Cl_2 extraction) to isolate the final product. The results are summarized in Table 1.

Table 1. Experimental conditions tested for the treatment of **1a** with phenylhydrazine **4** (R^3 = Ph)

Solvent	Equiv. of **4a**	T (°C)	T (h)	Work-up[b]	Result (Yield)[c]
MeOH	2	140 mw[a]	0.5	1	**3a** (50%)
	2	140 mw	0.5	2	**3a** (47%)
	2	reflux	24	1	**7a** (70%)
	1	140 mw	0.5	2	**7a** + **3a**
	1	140 mw	0.5	1	**7a** + **3a**
	2	reflux	24	2	**7a** (74%)
	2	60 mw	0.5	1	**7a** (23%)
Solvent free	1	140 mw	0.25	2	3a (39%)
	1	60 mw	0.25	2	7a (27%)
THF	1	60 mw	0.25	1	**7a** (7%)
	1	140 mw	0.25	1	**7a** impure
	1	140 mw	0.5	1	**7a** (9%)
	2	140 mw	0.25	1	**7a** (3%)
	2	reflux	24	1	**7a** (25%)
CH_2Cl_2	2	140 mw	0.5	1	**7a** (15%)

[a] microwave irradiation. [b] Work-up: (1) filtration, (2) CH_2Cl_2 extraction. [c] isolated compound, ^{1}H-NMR spectra of mother liquors present only signals corresponding to **7a** or **3a**, depending on the experiment, and excess of phenylhydrazine **4** (R^3 = Ph).

As it is clearly shown in Table 1, the corresponding isomer **2a** was not observed in any case. A factor with a great influence on the reaction is the temperature, thus for temperatures below 140°C the cyclization reaction did not take place and intermediate **7a** was obtained in all cases.

However, when the reaction is carried out at 140°C under microwave irradiation in MeOH using two equivalents of

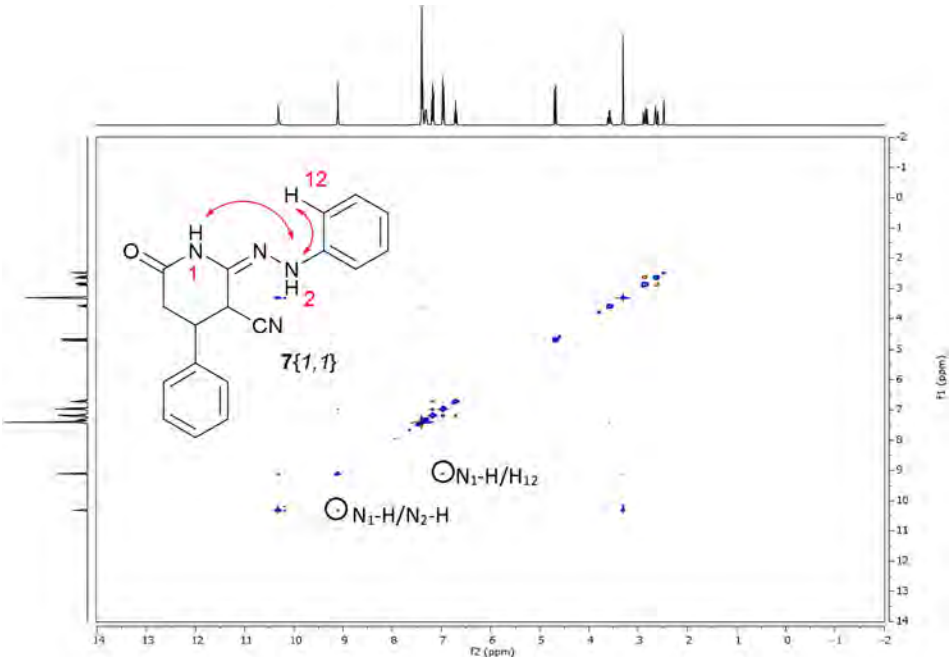

Figure 2. NOESY spectrum of intermediate **7 a.**

phenylhydrazine **4** (R^3 = Ph) the cyclization takes place and **3 a** is obtained. The structure of **3 a** and the product purity were established using the ^{1}H-NMR spectra. Thus, the signal appearing at 9.11 ppm (N–H) in the case of the intermediate **7 a** disappears and a singlet corresponding to the NH_2 group (2H) is observed at 5.28 ppm. The structural assignment was confirmed by NOESY spectroscopy, where correlation between NH_2 group and the phenyl groups are observed. Moreover, in the IR spectrum the band previously appearing at 2256 cm^{-1} corresponding to the C≡N stretching band of intermediate **7 a** disappears.

The cyclization of a sample of the isolated intermediate **7 a** was carried out in order to confirm the predicted reaction mechanism. A solution of **7 a** in methanol was heated at 140°C for 30 minutes under microwave irradiation to achieve cyclization into isomer **3 a.**

The results obtained confirmed our hypothesis that the initial substitution should be governed by the relative nucleophilicity of the two nitrogen atoms present in NH_2-NH-R^3. Consequently, in the case of phenylhydrazine **4** (R^3 = phenyl) the initial substitution proceeds through the NH_2 nitrogen, thus leading to isomer **3.**

However, this result is contrary to those described by Rodrigues-Santos *et al.*[5] who claimed that isomers **2** are always obtained. In order to cast light on such incongruence, we decided to extend the study to pyridones **1b–d** to determine the possible influence of the nature and position of substituents R^1 and R^2.

We started the study using pyridone **1 d** (R^1 = H, R^2 = *p*-MeO-C_6H_4) used as model compound by Rodrigues-Santos *et al.*[5] The reaction was carried out using conventional heating (24 h at reflux in MeOH) with phenylhydrazine **4** (R^3 = Ph) (2:1 molar excess). The reaction afforded intermediate **7 d** (R^1 = H, R^2 = *p*-MeO-C_6H_4) in 70% yield as in the case of pyridone **1 a** (see above). The structure was confirmed by IR and ^{1}H-NMR (see supporting information). Particularly revealing was the NOESY spectrum (see supporting information) which shows the same kind of correlations observed in **7 a.**

Cyclization of intermediate **7 d** as starting material was achieved upon heating in MeOH at 140°C under microwave irradiation and the cyclized compound **3 d** was obtained in 97% yield.

Finally, in order to definitively confirm the structure of **3 d**, single crystals were grown by vapor diffusion of water into 3 mL of a MeOH solution of 5 mg of **3 d.** The crystal structure was determined by single crystal X-ray diffraction. **3 d** crystallizes in monoclinic centrosymmetric space group P21/n. The ORTEP diagram and atomic numbering are given in Figure 3.

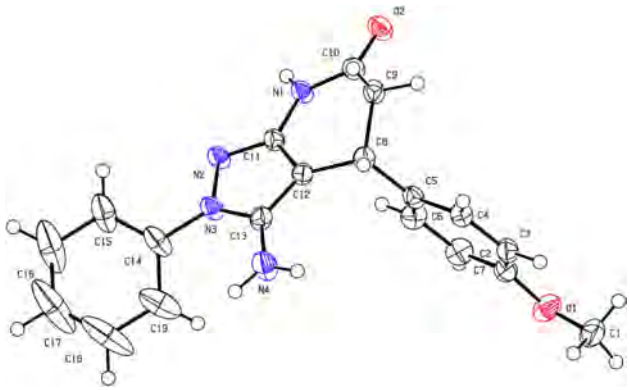

Figure 3. ORTEP diagram and atomic numbering of **3 d.**

Crystallographic data are summarized in supporting information.

The resulting structure clearly shows the presence of the phenyl substituent in position C2 of the pyrazole ring, thus confirming that the isomer obtained is **3 d.**

Further exploration of the synthesis of **3 d** showed that it can be directly obtained using a 2:1 molar ratio of **4** (R^3 = Ph) with respect to pyridone **1 d** under microwave irradiation at 140°C for 30 min in 85% yield.

To establish the general applicability of this synthetic methodology, we extended the reaction to two other pyridones: **1 b** (R^1 = Ph, R^2 = H) and **1 c** (R^1 = Me, R^2 = H). When the reactions with 2 equivalents of phenylhydrazine **4** (R^3 = Ph) were carried out at room temperature in MeOH the corresponding open intermediates **7 b** and **7 c** were obtained in 81% and 60% yield, respectively. The same reactions carried out at 140°C under microwave irradiation afforded **3 b** (48%) and **3 c** (58%), respectively (see supporting information).

Consequently, we can summarize the results obtained as follows (Scheme 3): a) when the reaction between pyridones **1** and phenylhydrazine **4** (R^3 = Ph) is carried out in MeOH (or other solvents) below 140°C, intermediates **7** are formed in 60–80% yield; b) such intermediates can be converted in the corresponding 2-aryl substituted 3-amino-2,4,5,7-tetrahydro-6*H*-pyrazolo[3,4-*b*]pyridin-6-ones **3** by heating in MeOH under microwave irradiation at 140°C in good yields (50-90%); and c) pyrazolopyridines **3** can be directly obtained using pyridones **1** and phenylhydrazine **4** (R^3 = Ph) heated in MeOH under microwave irradiation at 140°C in 40–60% yield. In no case we have even detected the regioisomeric pyrazolo[3,4-*b*]pyridines **2.**[5]

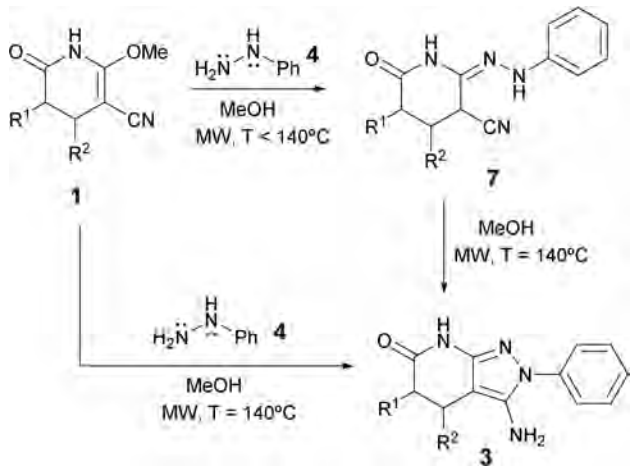

Scheme 3. Conversion of pyridones **1** in open intermediates **7** or pyrazolopyridines **3** depending on the reaction temperature.

Finally, to understand the high thermal level needed for the cyclization of intermediates **7**, we decided to determine the activation energies of the two steps involved in the formation of pyrazolopyridines **3:** a) substitution of the methoxy group present in pyridones **1** with phenylhydrazine **4** (R^3 = Ph) to afford intermediates **7**; and b) cyclization of intermediates **7** to yield pyrazolopyridines **3.**

Preliminary *ab-initio* calculations using Gaussian 09 already indicated that the second barrier is higher than the first one but the values obtained were both too high. Consequently, we decided to determine experimentally such barriers using differential scanning calorimetry (DSC) techniques. Thus, a 1:2 mixture of **1 c** and phenylhydrazine **4** (R^3 = Ph) in MeOH was introduced in a medium pressure stainless steel crucible and heated from 40°C to 160°C at different heating rates under a nitrogen stream. The activation energy was then determined using the kinetic methods of Ozawa[6] and Kissinger[7] to afford 15.6 ± 1.6 kcal·mol^{-1} and 14.3 ± 1.6 kcal·mol^{-1}, respectively.

Similarly, intermediate **7 c** was heated in absence of solvent in a standard aluminium crucible with a pierced lid from 120°C to 220°C at different heating rates under a nitrogen stream. The activation energy was determined using the kinetic methods of Ozawa,[6] Kissinger[7] and Kissinger-Akahira-Sunose.[8] The results obtained were 42.4 ± 2.3, 42.8 ± 2.4 and 40.6 ± 0.2 kcal·mol^{-1}, respectively. The ^{1}H-NMR spectrum of the contents of the standard aluminum crucible showed the complete transformation of intermediate **7 c** to pyrazolopyridine **3 c** (see supporting information).

These results are clearly compatible with our findings and show why the cyclization step must proceed at 140°C. In fact, the experimental activation energies obtained are in agreement with the observations of Rodríguez *et al.*[9] who established that reactions with activation energies below 20 kcal·mol^{-1} occur easily by conventional heating, while reactions with activation energies above 30 kcal·mol^{-1} cannot be performed under conventional heating or need highly polar solvents under microwave irradiation.

Consequently, we believe that Rodrigues-Santos *et al.*[5] mistook intermediates **7** for isomers **2** probably because the reaction temperature reached by their microwave for home-use was not high enough to allow the reaction to complete.

A literature search has revealed, in one side, that there are almost no examples of 2-aryl substituted pyrazolo[3,4-*b*] pyridines referable to **3** and, on the other side, that the reactions between cyano groups and NH_2-Ph groups (the mechanistic step needed for the cyclization step affording compounds **3**) are normally carried out using acid catalysis.

To sum up, the formation of compounds **3** cannot be qualified as an obvious reaction because it requires heating at 140°C in MeOH under microwave irradiation due to the very high activation energy involved in such process (around 42 kcal·mol^{-1}).

Conclusions

We have clearly shown that the treatment of pyridones **1a–d** with phenylhydrazine **4** (R^3 = Ph) in MeOH at temperatures below 140°C yields, independently of the nature and position of the substituents present in the pyridine ring, the corresponding open intermediates **7 a–d.** When the reaction is carried at 140°C under microwave irradiation, the corresponding pyrazolo [3,4-*b*]pyridines **3a–d** are always formed. In no case we have even detected the regioisomeric pyrazolo[3,4-*b*]pyridines **2.**[5] We have experimentally determined that the activation energy

of the cyclization step from intermediates **7** to pyrazolo[3,4-*b*] pyridines **3** is around 42 kcal·mol^{-1}. Such barrier is overcome due to the overheating of the intermediate **7** solution in MeOH at 140°C under microwave irradiation at 11 bar. We are currently routinely using this methodology for the production of libraries of pyrazolo[3,4-*b*]pyridines **3** and extending the study to methyl substituted hydrazine **4** (R^3 = Me).

Acknowledgements

E. Bou-Petit thanks the *Secretaria d'Universitats i Recerca* del *Departament d'Economia i Coneixement* de la *Generalitat de Catalunya* (2017 FI_B2 00139) and the European Social Funds for her predoctoral fellowship. N. Ferrer thanks Medichem for a predoctoral fellowship.

Conflict of Interest

The authors declare no conflict of interest.

Keywords: Activation energies · Cyclization · DSC · Microwave assisted synthesis · Pyrazolo[3,4-*b*]pyridin-6-ones

[1] E. S. Komarova, V. A. Makarov, V. G. Granik, C. Párkányi, *J. Heterocycl. Chem.* **2012**, *49*, 969–998.
[2] B. Martínez-Teipel, J. Teixidó, R. Pascual, M. Mora, J. Pujolà, T. Fujimoto, J. I. Borrell, E. L. Michelotti, *J. Comb. Chem.* **2005**, *7*, 436–448 and the references therein.
[3] J. L. Falcó, M. Lloveras, I. Buira, J. Teixidó, J. I. Borrell, E. Méndez, J. Terencio, A. Palomer, A. Guglietta, *Eur. J. Med. Chem.* **2005**, *40*, 1179–1187.
[4] ACE and JChem acidity and basicity calculator. https://epoch.uky.edu/ace/public/pka.jsp.
[5] C. E. Rodrigues-Santos, A. Echevarria, *Tetrahedron Lett.* **2011**, *52*, 336–340.
[6] T. Ozawa, *Bull. Chem. Soc. Jpn.* **1965**, *38*, 1881–1886.
[7] H. E. Kissinger, *Reaction Kinetics in Differential Thermal Analysis. Anal. Chem.* **1957**, *29*, 1702–1706.
[8] a) T. Akahira, T. Sunose, *Trans. Joint Convention of Four Electrical Institutes*, Paper No. 246, 1969; b) Research Report Chiba Inst. Technol. No.16, 22, 1971.
[9] A. M. Rodríguez, P. Prieto, A. de la Hoz, Á. Díaz-Ortiz, D. R. Martín, J. I. García, *ChemistryOpen* **2015**, *4*, 308–317.

Submitted: April 6, 2017
Accepted: April 21, 2017

Structural implications of the DFD-in domain in computer-aided molecular design of MAP kinase interacting kinase 2 inhibitors.

P. Salvador Gil 2015 Award in Chemistry (November 27th, 2015 in the Annual General Assembly of the AIQS)

E. Bou-Petit[1], J.I. Borrell[1], S. Ramón y Cajal[2] and R. Estrada-Tejedor[1,*]

[1]Grup d'Enginyeria Molecular, IQS School of Engineering, Universitat Ramon Llull. Via Augusta 390, 08017 Barcelona, Catalonia, Spain. [2]Department of Pathology, Vall d'Hebron University Hospital, Universitat Autònoma de Barcelona, Passeig Vall d'Hebron 119-129, 08035 Barcelona, Spain

Implicaciones estructurales del dominio DFD-in en el diseño molecular de inhibidores de la proteína MAP kinase interacting kinase 2.

Implicacions estructurals del domini DFD-in en el disseny molecular d'inhibidors de la proteïna MAP kinase interacting kinase 2.

RECEIVED: 17 FEBRUARY 2017. ACCEPTED: 31 MAY 2017

SUMMARY

Protein translation is a key process on cell development and proliferation that is often deregulated in cancer. MAP kinase interacting kinases 1 and 2 (Mnk1/2) play a pivotal role in regulating the cap-dependent translation through phosphorylation of eIF4E transcription factor. Thus, Mnk1/2 targeting have been proposed as a novel therapeutic strategy that would minimize side-effects in contrast to other therapies. For this reason, there is a growing interest in designing *in silico* new Mnk1/2 inhibitors which demands from reliable structural models. Interestingly, the catalytic domain of Mnk proteins are characterized by a DFD motif instead of the characteristic DFG motif of other kinases. However, Mnk2 structural models described in literature are DFG mutated and do not contain the activation loop. Molecular design techniques have been applied to obtain a structural model of the full wildtype Mnk2 protein including the activation loop. The effect of the loop on the interaction mechanism of well-known ligands has been evaluated. Obtained results suggest that the presence of the activation loop is determinant for the correct prediction of the active site and it is essential for the design of new inhibitors.

Keywords: Drug design; MNK2 inhibition; molecular docking.

RESUMEN

La traducción de proteínas es un proceso clave para el desarrollo y la proliferación celular que se encuentra desregulado en muchos cánceres. Las proteínas MAP kinase interacting kinases 1 and 2 (Mnk1/2) juegan un papel fundamental en la traducción *cap*-dependiente regulando la fosforilación del factor eIF4E y se han postulado como una diana terapéutica de gran interés para intentar minimizar los efectos secundarios de las terapias convencionales. Por este motivo, hay un interés creciente en el diseño *in silico* de nuevos inhibidores de Mnk1/2 que, en consecuencia, requiere de modelos estructurales fiables. El dominio catalítico de las proteínas Mnk presenta un motivo DFD que sustituye el motivo DFG característico de las proteínas quinasas. Sin embargo, en el caso particular de la Mnk2, los modelos estructurales disponibles en la bibliografía presentan la mutación DFG y les falta el *loop* de activación. Mediante técnicas de diseño molecular se ha obtenido un modelo completo de la proteína Mnk2 *wildtype* que incluye el *loop* de activación y se ha evaluado el efecto de éste sobre el mecanismo de interacción de ligandos conocidos. Los resultados obtenidos indican que la presencia del *loop* de activación es determinante para la correcta identificación del centro activo y se considera esencial para el diseño de nuevos inhibidores.

***Corresponding author: roger.estrada@iqs.url.edu**

Palabras clave: Diseño de fármacos; inhibición de MN2; docking molecular.

RESUM

La traducció de proteïnes és un procés clau per al desenvolupament i la proliferació cel·lular que es troba desregulat en molts càncers. Les proteïnes MAP kinase interacting kinases 1 and 2 (Mnk1/2) juguen un paper fonamental en la traducció cap-depenent mediant la fosforilació del factor eIF4E i han esdevingut una diana terapèutica de gran interès per intentar minimitzar els efectes secundaris de teràpies convencionals. Per aquest motiu, hi ha un interès creixent en el disseny *in silico* de nous inhibidors de Mnk1/2 que, en conseqüència, requereix de models estructurals fiables. El domini catalític de les proteïnes Mnk presenta un motiu DFD que substitueix el característic motiu DFG de les proteïnes cinases. No obstant, en el cas particular de la Mnk2, els models estructurals disponibles en la bibliografia presenten la mutació DFG i els manca el *loop* d'activació. Mitjançant tècniques de disseny molecular s'ha obtingut un model complet de la proteïna Mnk2 *wildtype* que inclou el *loop* d'activació i s'ha avaluat l'efecte d'aquest sobre el mecanisme d'interacció de lligands coneguts. Els resultats obtinguts indiquen que la presència del *loop* d'activació és determinant per a la correcta identificació del centre actiu i es considera essencial pel disseny de nous inhibidors.

Paraules clau: Disseny de fàrmacs; inhibició de MNK2; docking molecular.

INTRODUCTION

Overexpression of the components of the translation initiation machinery has been correlated to malignant transformation. The limiting eukaryotic translation initiation factor 4E (eIF4E) was found to be up-regulated in most human cancers[1] and has been related to poor prognosis[2]. Overexpression of eIF4E increases the translation of mRNAs with a structured 5' untranslated region (5' UTR) which are usually translated with low efficiency as they include transcription factors, growth factors, receptors and tyrosine kinases[2-6].

The mitogen-activated protein kinase (MAPK) interacting protein kinases (Mnks 1/2) are serine/threonine kinases that regulate the activity of proteins involved in diverse cellular functions through phosphorylation. Mnk inhibition decreases the levels of phosphorylated eIF4E and attenuates the expression of mRNA involved in cell proliferation becoming a potential strategy for the treatment of many cancers. Interestingly, experimental studies on Mnk1/2 knockout mice conclude that eIF4E phosphorylation is crucial for tumorigenesis but dispensable for normal cell development[7].

Design of new inhibitors to target Mnk proteins has become an interesting starting point for search of novel cancer therapies. In this regard, molecular modelling techniques have risen as an effective strategy to guide the drug design process. Unfortunately, limited data is available on known inhibitors commonly used as reference for drug design (Figure 1). Moreover, these molecules are planar heterocyclic systems that mimic the adenine moiety of ATP in order to act as ATP competitors and, therefore, present a low specificity for Mnks. In view of the lack of ligand-based information, structural information about the receptor becomes mandatory to allow the application of structure-based drug design.

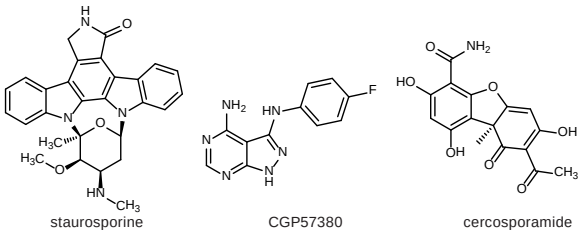

Figure 1. *Molecular structure of known Mnk1/2 inhibitors taken as reference in this study.*

Molecular structure of Mnk proteins has a strong resemblance to other protein kinases; they have a bilobed arrangement in which the N-terminal lobe contains the regulatory α-helix (αC), a twisted sheet of five antiparallel β-strands and a highly flexible glycine-rich loop which plays a key role in the ATP binding. The C-terminal lobe mainly consists on hydrophobic α-helical bundles and contains the elements required for phosphate transfer and for peptide substrate binding, including the activation loop. Interestingly, the ATP binding pocket is an hydrophobic cleft found abutting the hinge region. Both Mnk1/2 present a 80% identity of the active site despite the N-terminal lobe of Mnk1 is inclined 10° leaving a slightly more closed binding site[8]. However, Mnks present two unique features in contrast to tyrosine kinases[4, 11] consisting of (1) an specific insert in the catalytic domain (EAFSE in Mnk2) that seems to promote their activation or to guide the substrate recognition and (2) the replacement of the conserved DFG-motif for a particular DFD-motif (Figure 2).

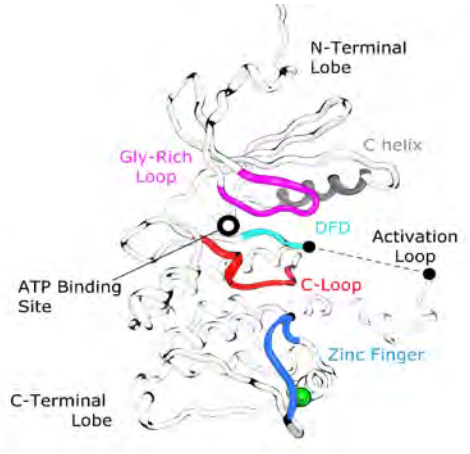

Figure 2. *General structure of the Mnk2 catalytic domain. The dotted line indicates that the activation loop has not been experimentally solved yet.*

DFD-motif is abutting the activation loop, which controls the binding of the ligand due to steric hindrance. In absence of ligands, Mnk2 adopts an inactive conformation (referred as the DFD-out conformation), sticking Phe227 into the ATP binding pocket and blocking the access to the binding site. When activated, the Phe227 leaves the hydrophobic pocket and flips clockwise about 180°. During this process, the salt bridge between Asp226 and Lys234 found on the DFD-out conformation is broken and a new salt bridge between Asp226 and Lys113 is formed (DFD-in conformation) [10].

To the best of our knowledge, the crystal structure of the wildtype (wt) Mnk2 protein presenting the DFD-in active conformation has not been described yet, and it is only available for the DFD-out conformation (PDB ID: 2AC3[9]). Most of the studies reported in literature are leaned on crystallographic structures of D228G Mnk2 mutants[12-15] (PDB ID: 2HW7[9], 2AC5[8]), considering that this mutation affects the conformation of Mnk2, but not the ATP binding and its kinase activity[8]. Noteworthy, none of the crystallographic models mentioned include information about the activation loop, thus it is usually neglected. This would lead to an over-simplistic model, particularly when molecular dynamics simulations suggested that DFD flip is directly associated with conformational changes in the activation loop[10, 16].

In this study we have applied molecular modeling techniques to generate an structural model of Mnk2 DFD-in conformation including the activation loop. Having available the three dimensional structure of Mnk2 protein allows the design of new inhibitors through the application of Structure-Based Drug Design (SBDD) methodologies. Moreover, the effect of the activation loop has been evaluated by predicting the interaction mechanism of well-known Mnk2 inhibitors (i.e. staurosporine, cercosporamide and CGP57380, see Figure 1) by means of molecular docking.

Computational details

Modelling the activation loop of the Mnk2 DFD-in conformation

Structure of the Mnk2 D228G mutant in the active conformation (PDB ID: 2HW7) was downloaded from the PDB and prepared by using Molecular Operating Environment (MOE2014.09[17]). Hydrogen atoms were added, minimized and protonation states were assigned, and crystallographic waters were removed.

This structure was used as reference to generate two additional structural models: (1) a model without the activation loop, obtained by manually removing the residues of the DFD-motif (D226-G228) included in 2HW7 and (2) a second model of the wildtype Mnk2 protein including the activation loop in the active conformation. To generate the latest model, residue G228 was de-mutated to recover the wildtype sequence. The tertiary structure of the activation loop (involving L229-C251 residues) was predicted *de novo* by applying the loop modeler module available in MOE. All calculations were conducted using the Amber12 forcefield. The best loop candidate was selected and energy minimized by molecular dynamics (MD) simulations, using AMBER software[18], to obtain the final model. Amber ff13 forcefield was used for the parameters of standard amino acids. The system was subjected to a first minimization including a 5000-step minimization of TIP3P water molecules followed by a 20000-step energy minimization of the entire system. The system was therefore heated to 300 K in 200 ps using the Langevin thermostat restraining the backbone atoms except the loop atoms using an 8 $kcal{\cdot}mol^{-1}{\cdot}Å^{-2}$ force constant. Pressure equilibration (1 atm) was performed for 1000 ps maintaining the restraints previously described. The SHAKE algorithm[19] was used throughout to restrain the bonds involving hydrogens and the Particle Mesh Ewald[20] method for long range electrostatic, while the short range interactions had a 10 Å cutoff radius. The production phase was extended to 20 ns defining a 2 fs time-step.

Molecular docking

Molecular docking was performed using AutoDock 4 and AutoDock Tools[21]on a 1.80 GHz Intel® Core™ i5-3337U processor with 4 GB RAM. A 126x126x126 Å grid was defined to perform a blind docking. Genetic Algorithms (GA) were used as docking search method, fixing the number of GA runs to 200, defining a population size of 500 and a maximum number of 2500000 evaluations. Evaluation of the results is performed by cluster analysis. Alternatively, MOE 2014.09 software was applied to include a flexible receptor into docking procedure (i.e. induced fit protocol). Docking poses are generated using the triangle matcher placement method (2000 poses) and scored using London ΔG scoring function and GBVI/WSA ΔG for rescoring (100 poses).

RESULTS AND DISCUSSION

Three models were considered for the evaluation of the activation loop effect: (1) the reported 2HW7 PDB structure, which contains the resolved structure for only few atoms of the activation loop and presents the DFG mutation, (2) the wildtype Mnk2 protein with the modelled loop and (3) 2HW7 without loop.

Two docking methods (rigid receptor and induced fit) were compared in order to discuss the relevance of the D228G mutation and the presence of the activation loop when studying the binding mechanism of drug candidates to Mnk2. For this purpose, we docked the reference compounds (i.e. staurosporine, cercosporamide and CGP57380, see figure 1) on the three Mnk2 models.

Molecular docking protocol was validated (RMSD < 0.25 Å) by predicting the binding mechanism of staurosporine and comparing the result to the crystal structure of staurosporine complexed to the Mnk2 D228G mutant structure available in the PDB (2HW7).

Rigid docking

According to the results, the recognition of the active site by the ligands could be conditioned by the

presence of the activation loop when applying rigid docking and the protein structure was fixed.

Cluster analysis showed that staurosporine was able to mostly recognize the active site in all models, suggesting that the presence of the loop did not induce a remarkable effect on the location of the ligand. On the contrary, the presence of the activation loop hindered the access to the active site for cercosporamide and CGP57380. The combined effect of activation loop and the DFD motif conformations blocked the active site abutting the C-helix, moving their preferred binding site from the ATP binding site to the helix region at the C-terminal lobe (Figure 3).

From Figure 3 it can be seen that an appreciable percentage of conformations are located in the ATP binding site, regardless of the presence of the activation loop. Residues included in the active site were defined by proximity (4.5 Å) to the crystallized staurosporine-Mnk2 complex available in literature. Nevertheless, conformations located into the active site do not correspond to the best ranked conformations in terms of the scoring function and this could lead to confusing results.

Although staurosporine preferentially bounds to the ATP binding site, the spatial orientation of the most stable binding conformations predicted with and without the activation loop were slightly different (Figure 4). Structural differences could be appreciated when comparing the binding mechanism, obtaining two flipped conformations according to a symmetry axis, with comparable score.

Figure 4. *Comparison between the most stable staurosporine conformations predicted by docking when considering the Mnk2 protein without activation loop (white) and containing a de novo modelled activation loop (black). (A) Position of the best ranked staurosporine conformations within the Mnk2 protein, corresponding to the active site. (B) Comparison between the spatial orientations of both conformations obtained.*

According to these results, the activation loop may have a pivotal role in drug recognition. Moreover, rigid docking did not allowed to obtain a correlation between the active site recognition and the scoring function value. This situation gives rise to unrealistic docking results and we hypothesized the need of including protein flexibility in the study.

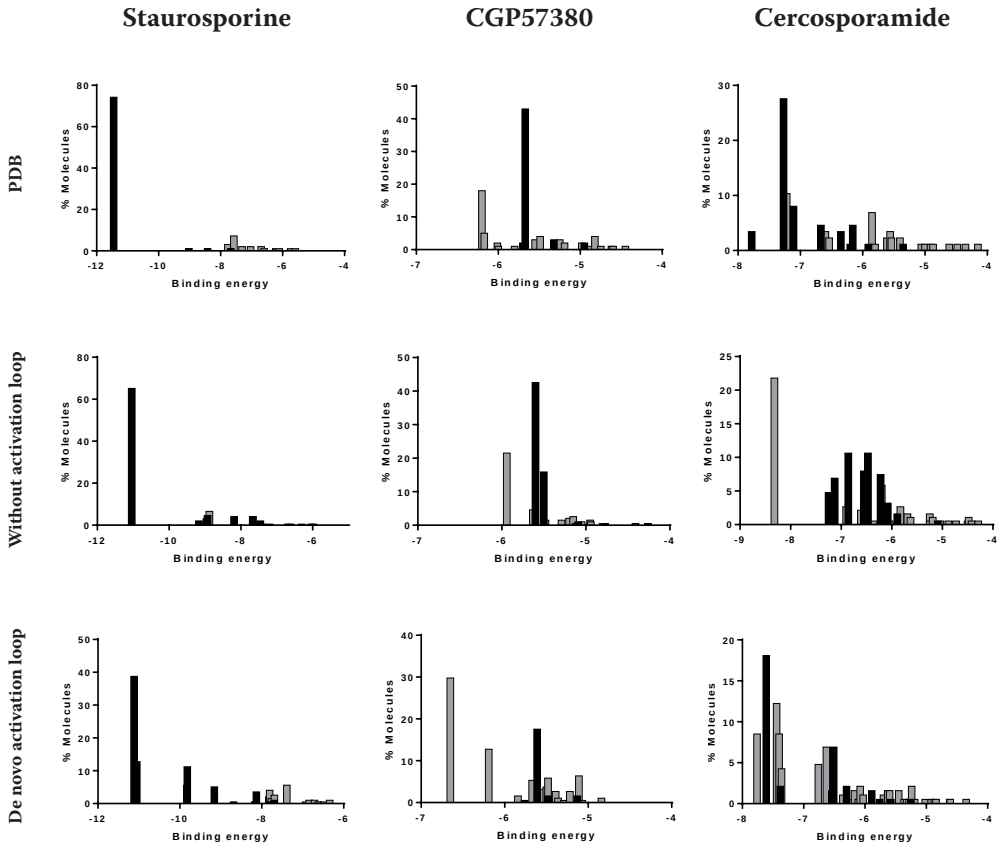

Figure 3. *Cluster analysis from rigid docking. Molecules are divided in two groups depending on where they bind: the active site (black) or other parts of the protein, usually the α-helixes (grey).*

Induced fit docking

Induced fit docking revealed that the flexibility of the activation loop may contribute to guide ligands towards the active site. Interestingly, reference compounds showed a similar behavior in all models when allowing receptor flexibility. Ligands tend to bind to the external part of the β-sheets in absence of the activation loop. When a small part of the loop is present (corresponding to the structure directly obtained from the PDB), more conformations are found in the helixes despite some conformations bind into the active site.

In the presence of the modelled loop a higher percentage of conformations end up in the ATP binding site. The modelled loop guides molecules to the Glycine rich loop and avoids binding to the C-helix. Interestingly, the conformations with the best score are those located in the ATP binding site and conformations with a lower score bind to helixes. The distribution of docking conformations obtained for each model is included in Figure 5.

Cluster analysis revealed that the model including the activation loop *de novo* modeled is the one that allows to lead the higher number of conformations with higher score within the active site (Table 1). The flexibility of the activation loop is determinant in order to obtain these results.

Table 1. *Percentage of molecules bound to the Mnk2 ATP binding site.*

PDB	Staurosporine	CGP57380	Cercosporamide
	28%	20%	12%
Without activation loop	18%	15%	11%
De novo activation loop	33%	36%	22%

In order to make the visualization of these results easier, the three dimensional coordinates of each Mnk2 residue were projected into the H^2 hyperbolic plane. This procedure allows the representation of multidimensional points into a bidimensional space in which the distance between projected points increase exponentially with the radii by changing the metric definition (in this case, using Poincaré's disk model) [22]. Residues were colored according to the protein region and their positions were compared with the location of staurosporine conformations (Figure 6).

As expected, results showed that a higher number of staurosporine conformations are located close to the DFD motive and the ATP binding site. It is a worth of attention the effect of the activation loop on the Mnk2 projection, which modifies the conformation of the protein and induces a change into staurosporine distribution reducing binding affinity towards the β-sheets and the C-helix and concentrating conformations on the active site.

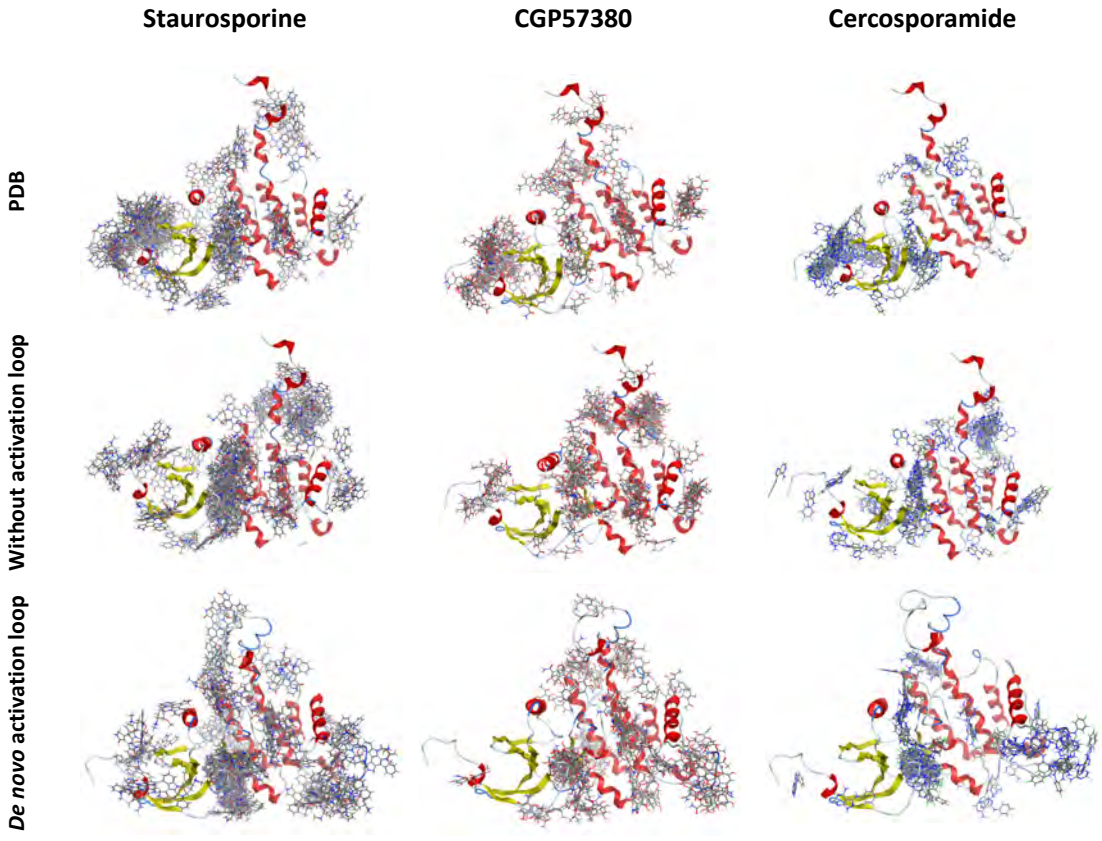

Figure 5. *Graphical representation of the conformations obtained by induced fit docking.*

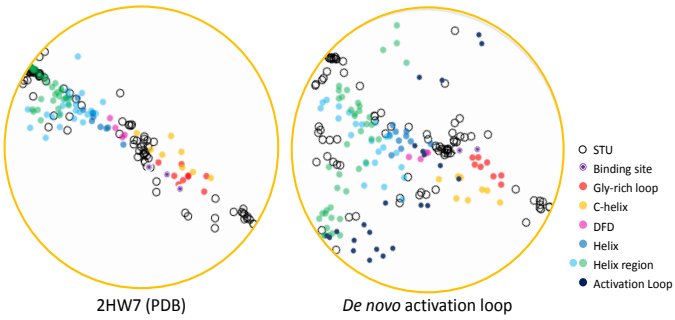

Figure 6. *Hyperbolic projection of Mnk2 residues resulting from flexible docking on PDB (2HW7) and the structure with the modelled loop.*

These results are in disagreement with methodologies commonly reported in literature for designing new Mnk2 inhibitors. Most of research articles directly apply molecular docking on the mutated Mnk2 structure available in the PDB. Our findings suggest that these models may be over simplistic and they could lead to unrealistic results. The presence of the activation loop and considering the flexibility of the receptor may be crucial for the correct description of the Mnk2-ligand complex and both should be considered when applying structure-based drug design techniques.

CONCLUSIONS

The effect of the activation loop on predicting the preferred binding site of Mnk2 inhibitors has been evaluated by molecular docking. The wildtype Mnk2 structure in the DFD-in conformation has been modeled by modifying the structure of Mnk2 D228G mutant available in the PDB. The three dimensional structure of the activation loop has been predicted computationally by *de novo* design methodologies.

The presence of the activation loop was essential to lead ligands towards the active site and receptor flexibility was required in order to obtain reliable results. Thus, obtained results suggest that the presence of the activation loop is determinant for the correct prediction of the active site of known ligands in docking procedures and it should be therefore considered in molecular design of new Mnk2 inhibitors.

ACKNOWLEDGMENTS

The authors thankfully acknowledge. the AIQS for the award of Pare Salvador Gil prize. Authors thankfully acknowledge. the computer resources at Minotauro and technical support provided by Barcelona Supercomputing Center (BCV-2016-1-0002, BCV-2015-3-0009). E. Bou-Petit thanks the *Secretaria d'Universitats i Recerca del Departament d'Economia i Coneixement de la Generalitat de Catalunya* (2016FI_B100054) and the European Social Funds for her predoctoral grant.

REFERENCES

1. Wheater, M. J.; Johnson, P. W.; Blaydes, J. P. The role of MNK proteins and eIF4E phosphorylation in breast cancer cell proliferation and survival. Cancer Biol. Ther. **2010**, 10, 728–735.
2. Ozretic, P.; Bisio, A.; Inga, A.; Levanat, S. The growing relevance of cap-independent translation initiation in cancer-related genes. Period. Biol. **2012**. 114, 471–478.
3. Diab, S.; Kumarasiri, M.; Yu, M.; Teo, T.; Proud, C.; Milne, R.; Wang, S. MAP Kinase-Interacting Kinases—Emerging Targets against Cancer. Chem. Biol. **2014**. 21, 441–452.
4. Hou, J.; Kam, F.; Proud, C.G.; Wang, S. Targeting Mnks for Cancer Therapy. Oncotarget. **2012**. 3, 118–131.
5. Furic, L.; Rong, L.; Larsson, O.; Koumakpayi, I.H.; Yoshida, K.; Brueschke, A.; Petroulakis, E.; et al. eIF4E phosphorylation promotes tumorigenesis and is associated with prostate cancer progression. Proc. Natl. Acad. Sci. **2010**, 107, 14134–14139.
6. Wendel, H.-G.; Silva, R.L.; Malina, A.; Mills, J.R.; Zhu, H.; Ueda, T.; Watanabe-Fukunaga, R.; et al. Dissecting eIF4E action in tumorigenesis. Genes Dev. **2007**, 21, 3232–3237.
7. Ueda, T.; Sasaki, M.; Elia, A.J.; Chio, I.I.; Hamada, K.; Fukunaga, R.; Mark, T.W. Combined deficiency for MAP kinase-interacting kinase 1 and 2 (Mnk1 and Mnk2) delays tumor development. Proc. Natl. Acad. Sci. U. S. A. **2010**, 107, 32, 13984–13990.
8. Jauch, R.; Jäkel, S.; Netter, C.; Schreiter, K.; Aicher, B.; Jäckle, H.; Wahl, M.C. Crystal Structures of the Mnk2 Kinase Domain Reveal an Inhibitory Conformation and a Zinc Binding Site. Structure. **2005** 13, 1559–1568.
9. Jauch, R.; Cho, M.; Jäckel, S.; Netter, C.; Schreiter, K.; Aicher, B.; Zweckstetter, M.; Jäckle, H.; Wahl, M.C. Mitogen-activated protein kinases interacting kinases are autoinhibited by a reprogrammed activation segment. EMBO J. **2006**, 25, 4020–4032.
10. Hou, J.; Teo, T.; Sykes, M. J.; Wang, S. Insights into the Importance of DFD-Motif and Insertion I1 in Stabilizing the DFD-Out Conformation of Mnk2 Kinase. ACS Med. Chem. Lett. **2013**, 4, 736–741.
11. Cargnello, M.; Roux, P.P. Activation and Function of the MAPKs and Their Substrates, the MAPK-Activated Protein Kinases. Microbiol. Mol. Biol. Rev. **2011**, 75, 50–83.
12. Teo, T.; Yang, Y.; Yu, M.; Basnet, S. K.; Gillam, T.; Hou, J.; Schmid, R.M.; Kumarasiri, M.; Diab, S.; Albrecht, H.; Sykes, M.J.; Wang, S. An integrated approach for discovery of highly potent and selective Mnk inhibitors: Screening, synthesis and SAR analysis. Eur. J. Med. Chem. **2015**, 103, 539–50.
13. Wu, H.; Wu, H. S.; Wang, A.; Weisberg, E.L.; Chen, Y.; Yun, C.; Wang, W.; Liu, Y.; et al. Disco-

very of a BTK/MNK dual inhibitor for lymphoma and leukemia. Leukemia. **2016**. 30, 173–181.
14. Yu, M.; Li, P.; Basnet, S.K.; Kumarasiri, M.; Diab, S.; Teo, T.; Albrecht, H.; Wang, S. Discovery of 4-(dihydropyridinon-3-yl)amino-5-methylthieno[2,3-d]pyrimidine derivatives as potent Mnk inhibitors: synthesis, structure–activity relationship analysis and biological evaluation. Eur. J. Med. Chem.**2015**. 95, 116–126.
15. Oyarzabal, J.; Zarich, N.; Albarran, M.I.; Palacios, I.; Urbano-Cuadrado, M.; Mateos, G.; Raymundo, I.; Rabal, O.; et al. Discovery of Mitogen-Activated Protein Kinase-Interacting Kinase 1 Inhibitors by a Comprehensive Fragment-Oriented Virtual Screening Approach. J. Med. Chem. **2010**, 53, 6618–6628.
16. Kumarasiri, M.; Teo, T.; Wang, S. Dynamical insights of Mnk2 kinase activation by phosphorylation to facilitate inhibitor discovery. Future Med. Chem.**2015**. 7, 91–102.
17. Chemical Computing Group Inc. Molecular Operating Environment (MOE). **2014**, 2014.09.
18. Case, D. A.; Berryman, J. T.; Betz, R. M.; Cai, Q.; Cerutti, D. S., Cheatham, T. E. AMBER 14. University of California, San Francisco, **2014**.
19. Ryckaert, J.P.; Ciccotti, G.; Berendsen, H.J. Numerical integration of the cartesian equations of motion of a system with constraints: molecular dynamics of n-alkanes. J. Comput. Phys.**1997**, 23, 327–341.
20. Darden, T.; York, D.; Pedersen, L. Particle mesh Ewald: An N ·log(N) method for Ewald sums in large systems. J. Chem. Phys. **1993**, 98, 10089–10092.
21. Morris, G. M.; Huey, R.; Lindstorm, W.; Sanner, M.F.; Belew, R.K.; Goodsell, D.S.; Olson, A.J. AutoDock4 and AutoDockTools4: Automated docking with selective receptor flexibility. J. Comput. Chem. **2009**, 30, 2785–2791.
22. Estrada, R.; Nonell, S.; Teixidó, J. Changing the way of viewing QSAR methods: the application of hyperbolic projection in medicinal chemistry. Rev. la Soc. Catalana Química. **2012**, 11, 61–67.